AWARD NUMBER: W81XWH-13-1-0233

TITLE: Development and Translation of Hybrid Optoacoustic/Ultrasonic Tomography for Early Breast Cancer Detection

PRINCIPAL INVESTIGATOR: Fatima Anis

CONTRACTING ORGANIZATION: Washington University
                                        Saint Louis, MO 63130

REPORT DATE: September 2014

TYPE OF REPORT: Annual

PREPARED FOR: U.S. Army Medical Research and Materiel Command
                                Fort Detrick, Maryland 21702-5012

The views, opinions and/or findings contained in this report are those of the author(s) and should not be construed as an official Department of the Army position, policy or decision unless so designated by other documentation.

		Form Approved
REPORT DOCUMENTATION PAGE		*Form Approved* *OMB No. 0704-0188*

Public reporting burden for this collection of information is estimated to average 1 hour per response, including the time for reviewing instructions, searching existing data sources, gathering and maintaining the data needed, and completing and reviewing this collection of information. Send comments regarding this burden estimate or any other aspect of this collection of information, including suggestions for reducing this burden to Department of Defense, Washington Headquarters Services, Directorate for Information Operations and Reports (0704-0188), 1215 Jefferson Davis Highway, Suite 1204, Arlington, VA 22202-4302. Respondents should be aware that notwithstanding any other provision of law, no person shall be subject to any penalty for failing to comply with a collection of information if it does not display a currently valid OMB control number. **PLEASE DO NOT RETURN YOUR FORM TO THE ABOVE ADDRESS.**

1. REPORT DATE September 2014	2. REPORT TYPE Annual	3. DATES COVERED 1 Sep 2013 - 31 Aug 2014
4. TITLE AND SUBTITLE Development and Translation of Hybrid Optoacoustic/ D Ultrasonic Tomography for Early Breast Cancer Detection		5a. CONTRACT NUMBER
		5b. GRANT NUMBER W81XWH-13-1-0233
		5c. PROGRAM ELEMENT NUMBER
6. AUTHOR(S) Fatima Anis E-Mail: fatimaanis@seas.wustl.edu		5d. PROJECT NUMBER
		5e. TASK NUMBER
		5f. WORK UNIT NUMBER
7. PERFORMING ORGANIZATION NAME(S) AND ADDRESS(ES) Washington University, Sponsored Research Services, Vice Chancellor for Research, Campus Box 1054, One Brookings Drive, St. Louis MO, 63130-4862		8. PERFORMING ORGANIZATION REPORT NUMBER
9. SPONSORING / MONITORING AGENCY NAME(S) AND ADDRESS(ES) U.S. Army Medical Research and Materiel Command Fort Detrick, Maryland 21702-5012		10. SPONSOR/MONITOR'S ACRONYM(S)
		11. SPONSOR/MONITOR'S REPORT NUMBER(S)

12. DISTRIBUTION / AVAILABILITY STATEMENT

Approved for Public Release; Distribution Unlimited

13. SUPPLEMENTARY NOTES

14. ABSTRACT

The broad objective of the proposed research is to develop an optimized system design and associated image reconstruction algorithms for a hybrid three-dimensional (3D) breast imaging system that combines OAT and UST. Significant progress has been made during last year in accomplishing the specific tasks for this project. In the past year, I (i) developed time-of-flight extraction algorithms to perform USCT, (ii) developing image reconstruction algorithms for USCT, (iii) developed iterative image reconstruction OAT algorithms (iv) developed accelerated OAT algorithm to enable 3D image reconstruction for breast imaging, (v) evaluated and validated algorithms by computer simulation studies and experimental phantom studies.

15. SUBJECT TERMS
Ultrasound Computed tomography, Optoacoutics Tomography, Breast Imaging, Iterative Image reconstruction algorithms, Bent-Ray USCT, GPU-accelerated algorithms

16. SECURITY CLASSIFICATION OF:			17. LIMITATION OF ABSTRACT	18. NUMBER OF PAGES	19a. NAME OF RESPONSIBLE PERSON USAMRMC
a. REPORT Unclassified	b. ABSTRACT Unclassified	c. THIS PAGE Unclassified	Unclassified	80	19b. TELEPHONE NUMBER *(include area code)*

Standard Form 298 (Rev. 8-98)
Prescribed by ANSI Std. Z39.18

Table of Contents

1. Introduction:

The broad objective of the proposed research is to develop an optimized system design and associated image reconstruction algorithms for a hybrid three-dimensional (3D) breast imaging system that combines OAT and UST. I have made excellent progress during last year in accomplishing the specific tasks for this project. In the past year, my research has primarily been focused on (i) developing time-of-flight extraction algorithms to perform USCT, (ii) developing image reconstruction algorithms for USCT, (iii) developing OAT algorithms (iv) accelerating OAT algorithm to enable 3D image reconstruction for breast imaging, (v) evaluating and validating algorithms by computer simulation studies and experimental phantom studies.

2. Keywords:

Ultrasound imaging, optoacoustic imaging, photoacoustic imaging, iterative image reconstruction, nonlinear optimization, breast imaging, GPU acceleration

3. Overall Project Summary

Task 1: Construct a computational model of the OAT/UST imager and identify optimal system geometries:

Computational modeling of the proposed imager:

Imager development is based on comprehensive computer models of OAT and UST. The system design studies are conducted concurrently with the development of the image reconstruction algorithms so that they can be informed and refined jointly.

Optimization studies:

I have conducted numerical studies to obtain an optimal imager design. The ultrasound tomographic image quality depends strongly on the distribution and number of emitters and transducers pairs. Moreover, image quality also depends on the number of tomographic views. These parameters have to be carefully chosen to obtain a feasible experimental design. Optimization studies were performed to determine the number of emitters and tomographic views for a fixed receiver's array. To obtain 3D SOS distribution, the emitters will be distribution on a planar surface.

Task 2: Development of reconstruction methods for sparse-array 3D UST

Reconstruction of SOS distribution:

Iterative image reconstruction algorithms have been developed to reconstruct the SOS distribution. These algorithms have also been validated for experimental phantom studies. To perform USCT, measured time-of-flight (TOF) was extracted from the measured signals of the transducer elements.

Time-of-flight (TOF) extraction of the transmission ultrasound signals: I utilized geometrical acoustic-based ray theory to establish a non-linear model that relates the measured TOF values to speed of sound (SOS) distribution. To solve this nonlinear optimization problem, we needed to extract time-of-flight (TOF) from the measured signal. This is a very important

pre-processing step for good image quality. In search of the best TOF extraction technique, six TOF extraction algorithms have been implemented and compared: (i) envelope-detection method, (ii) picking the max value of filtered signal, (iii) AIC-method, (iv) weighted-AIC picker, (v) cross-correlation method, and (vi) thresholding method from windowed and filtered signal [1]. These methods were investigated for both the computer simulation by adding different levels of noise and the experimental data (provided by Tomowave Laboratories Inc., Houston TX).

Figure 1: (a) Numerical breast phantom; (b) image reconstructed using adjoint-state method; (c) image reconstructed using bent-ray algorithm; (d) plot corresponding to vertical line in (a); (e) plot corresponding to horizontal line in (a). To have a fair comparison between two methods no regularization has been used in both methods.

Bent-Ray method: Algorithms are developed for reconstructing the SOS distribution of breast from knowledge of time-of-flight (TOF) measurements of the transmission ultrasound signals. Utilizing the geometrical acoustic-based ray theory, a non-linear model has been established that relates the measured TOF values to the SOS distribution.

For a given SOS distribution, numerically solution of the Eikonal equation yielded the ray paths. An iterative reconstruction method was developed for inverting the resulting system of equations that alternatively updates the estimates of the SOS and ray paths, minimizes a regularized cost function to obtain the final estimate of the SOS [2].

Adjoint-State Method: I also investigated a partial differential equation-based Eulerian approach to travel-time tomography as an alternative approach [3]. The work on comparison of the Adjoint-State Method are Ray-tracing algorithm was presented in SPIE Photonics West, 2014 and SPIE Medical Imaging 2014. For detail implementation of this algorithm please see attached proceedings paper. The waveform inversion method for SOS reconstruction has also been explored in the group. In this regard, Adjoint-State method provides a suitable initial SOS distribution to aid waveform inversion method.

I performed several numerical studies to compare bent-ray and adjoint-state method.

Tumor Diameter (mm)	X (FWHM) (mm)	Y (FWHM) (mm)	SOS (Actual 1600 m/s)	Error (%)
12	12	11.75	1598.2	0.11
10	9.75	9.5	1598.3	0.1063
8	7.75	7.25	1603.1	-0.194
6	7.0	6.75	1582.9	1.068
4	6.5	6	1560.0	2.5

Table 1: Performance of the adjoint-state method has been evaluated be performing many numerical simulations studies very varying tumor sizes. The adjoint-state method --- performs well for smooth SOS distributions --- can give accurate estimate of the size and SOS value for tumors ranging in 6 mm to 12 mm tumor sizes.

Figure (1) shows the comparison of the two methods for a numerical breast phantom. This numerical study was performed for a ring scanner consisting of 256 transducer elements. In another study, I varied the tumor size and performed image reconstruction to access tumor detectability using adjoint-state method. Table (1) summarizes results from this study. It can be
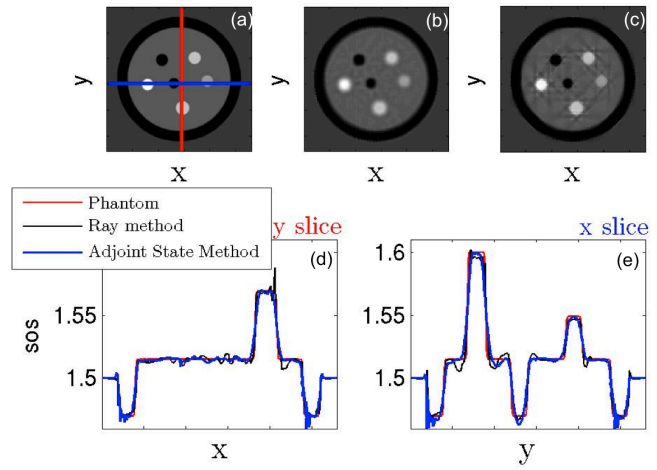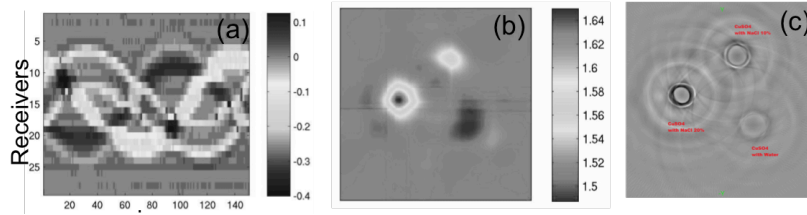
Figure 2: (a) Delta-TOF for the experimental three-tube phantom; (b) USCT image reconstructed using adjoint-state method; (c) OAT image

seen that the tumors with diameter large than 4 mm can be characterized using adjoint-state method.

The method was also validated for the experimental phantom studies. In this study, the pressure signals were recorded using a transducer array consisting of 64 elements and a single Laser Induced Source placed opposite to the middle transducer. The data was recoded for 150 views. The experimental phantom consisted of three tubes at varying salt concentration to exhibit different acoustic and optical properties. Results are shown in Figure (2) for both the SOS distribution and optical absorbed energy density.

Reconstruction of reflectivity: An algorithm has been developed to produce reflectivity maps. These algorithms are based on the Synthetic Transmit Aperture (STA) approach [4]. This method utilizes multiple elements or a single source to produce the spherical waves and the whole image is being reconstructed for each emitted signal. The final reflectivity map is obtained by accumulating these individual images. It has been shown that the STA method improves SNR. This method is especially useful in our current study because we are using laser induced ultrasound emitter (LUS), which produce spherical waves.

Task 3: Ultrasound-assisted OAT image reconstruction:

Development of imaging models and reconstruction algorithms: An interpolation-based discrete-discrete imaging model has been implemented to perform 3D OAT for breast imaging [5]. In the new implementation, an unmatched back projection (or pixel-driven) scheme has been used and validated in computer simulations studies. This algorithm is **five times** more efficient than the ray-driven back-projection and allows to perform iterative image reconstruction for large fields-of-views, making it very suitable for breast imaging. To efficiently mitigate data incompleteness, noise, and model error, I investigated the least-squares objective regularized by a TV-norm penalty. I implemented the fast iterative shrinkage/thresholding algorithm (FISTA) to minimize cost function with TV regularization [6].

GPU implementation of image reconstruction algorithms: Improved GPU-based implementations of a numerical imaging model and its adjoint have been developed for use with general gradient-based iterative image reconstruction algorithms. Particularly, two types of computation-reduced discretization methods have been employed; a parallel fast GPU-based Fourier transform (FFT) algorithm was employed to accelerate the calculation of the temporal convolution with ultrasonic transducer responses; and a volume-reduction method is proposed to reduce the computation for applications with irregular field-of-view (breast imaging). The results suggest that the proposed implementation is more than **five times** faster than previous implementations for a single GPU. In addition, the algorithm has also been developed to use multiple GPUs further reducing the computational time. The work will be presented in SPIE Photonics West, 2015.

4

Task 4: Validate prototype imager and image reconstruction algorithms

Phantom imaging studies: The imager and algorithm designs have been informed and evaluated by use of experimental studies for well-characterized multi-modality phantoms conducted at TomoWave Laboratories under Dr. Oraevsky. We used phantoms that have tumors located at different depths and have different optical absorption properties to quantify the sensitivity of the OAT system. Simplified versions of the phantoms will be imaged for characterizing the spatially variant spatial resolution and noise properties of the reconstructed images.
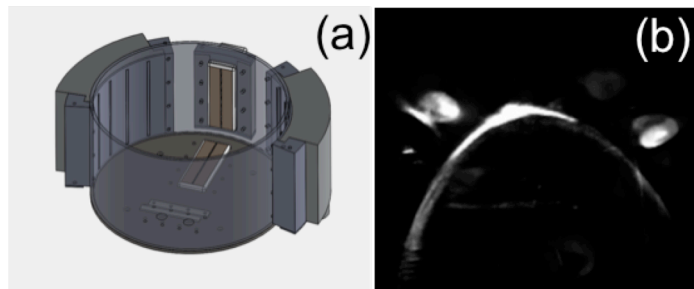

Figure 3: (a) LOUIS-3DB imaging module, (b) 3D rendered reconstructed image from experimental phantom study. The image is obtained using accelerated iterative image reconstruction algorithm. Both tumor inserts and blood vessel phantom are clearly visible in the reconstructed image.

4. Key Research Accomplishments:

Accelerating three-dimensional iterative image reconstruction algorithm: One of the key research accomplishment was the successful development of accelerated iterative image reconstruction algorithm for 3D OAT imaging. The task to perform 3D OAT breast imaging presents many challenges. One of the challenge is to account for large field-of-view. In a typical study, image reconstruction volume is 120 x 120 x 90 mm^3 and the existing iterative image-reconstruction algorithms present non-practical image reconstruction durations (days to obtain a single high-resolution image). Analytical algorithms, are efficient e.g. filter-back project (FBP), cannot account for data inconsistencies, model error, and noise in the data. This makes the accelerated
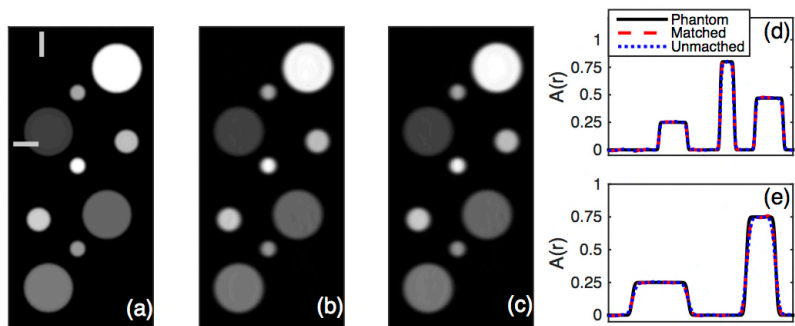

Figure 4: Slices for (a) original phantom (b) reconstructed image using the original interpolation-based algorithm with matched back projection scheme; (c) reconstruction image using accelerated algorithm, which is 20-times faster and exhibits same image quality; (d) line plot corresponding to vertical line in (a); (e) profile for horizontal line in (a) for (a) (solid line), (b) (dashed line) and (c) (dotted line) respectively.

image reconstruction algorithm very important milestone of the proposed project and will also benefit the optoacoustic tomography research field. Figure (4) shows results for a numerical phantom study for the accelerated interpolation-based imaging model.

5. Conclusion

I will continue to improve efficiency and accuracy of the reconstruction algorithms for USCT and OAT to perform breast imaging. Algorithms to reconstruct attenuation will also be developed. I will perform image reconstruction for clinical studies as soon as clinical data becomes available and will use the experimental study to investigate and improve the imaging

algorithms and imager design. Future studies will also be focused on developing task-based optimization studies for OAT and USCT next generation imager design. I will also develop algorithms to perform USCT-assisted OAT imaging.

6. Publications, Abstracts, and Presentations

1a. Waveform Inversion with Source Encoding for Breast Speed-of-Sound Reconstruction in Ultrasound Computed Tomography (submitted)
Authors: Kun Wang, Thomas Mathew, Fatima Anis, Cuiping Li, Neb Duric, and Mark Anastasio
Journal: IEEE Transaction on Medical Imaging

1b*. Investigation of the adjoint-state method for ultrasound computed tomography: a numerical and experimental study
Authors: Fatima Anis, Yang Lou, Andre Conjusteau, Sergey Ermilov, Alexander Oraevsky and Mark A. Anastasio
Conference: SPIE Photonics West- 2014, San Francisco CA

2b- Investigation of a method for laser-induced ultrasound tomography that eliminates the need for ray-tracing
Authors: Fatima Anis, Yang Lou, Andre Conjusteau, Sergey Ermilov,
Alexander Oraevsky and Mark A. Anastasio
Conference: SPIE Medical Physics- 2014, San Diego CA

3b- **Title:** Accelerated iterative image reconstruction in three-dimensional optoacoustic tomography
Authors: Fatima Anis, Yang Lou, Kun Wang, Richard Su, Tanmayi Oruganti, Andre Conjusteau, Sergey Ermilov, Alexander A. Oraevsky and Mark A. Anastasio
Conference: SPIE Photonics West, 2015

4b- **Title:** Waveform Inversion with Source Encoding for Breast Speed-of-Sound Reconstruction in Ultrasound Computed Tomography
Authors: Kun Wang, Thomas Mathew, Fatima Anis, Cuiping Li, Neb Duric, and Mark Anastasio
Conference: SPIE Medical Physics, 2015

7. Training

The year has been very fruitful as I continue to benefit from many scholarly activities and kept adding to my skills as imaging scientist.

1- **Attending course (E62 BME 500 67):** In Fall 2014, I participated in BME course on the imaging science. The class held weekly for two hours. Some of the study topics included continuous and discrete object representations, imaging operators, image statistics, imaging quality assessment, ideal observer, Hotelling observers and imaging errors. The course provided me with a formal training as biomedical image scientist.

2- **Conferences:**
   i- SPIE Photonics West, 2014 San Francisco CA: The conference is the major international meeting held annually for the optoacoustic/photoacpustic imaging. I

attended this meeting and was greatly benefited from the presentation and poster sessions as well as constructive meetings with the Prof. Oraevsky and his team about the hybrid OAT/ USCT breast imager.

ii- SPIE Medical Imaging, 2014, San Diago CA: This conference is another major international conference, which holds annually and covers broad range of topics concerning medical imaging and diagnostics. I was specially benefited from many talks and poster presentations about the image quality assessment. Moreover, the dedicated Ultrasonic Imaging and Tomography sessions on ultrasound imaging provided me with a great opportunity to learn about ultrasound tomography in medical imaging.

3- **Visiting TomoWave Inc, Houston TX:**
I visited TomoWave Inc. in December 2013. During the visit, I benefited from lab tours and learned about practical aspects of OAT/USCT imaging.

4- **Algorithm development and GPU computing:** I continued to establish more skills towards algorithm development. One of the major achievements towards this end was to learn CUDA programming from other group members. This training will continue to benefit me through the remainder of the project.

8. Reportable Outcomes
Nothing to report

9. Other Achievements
Nothing to report

10. References

[1] C. Li, L. Huang, N. Duric, H. Zhang, and C. Rowe, "An improved automatic time-of-flight picker for medical ultrasound tomography," Ultrasonics, vol. 49, no. 1, pp. 61–72, 2009.
[2] A. Hormati, I. Jovanovi, O. Roy, and M. Vetterli, "Robust ultrasound travel-time tomography using the bent ray model," Proc. SPIE, vol. 7629, 2010, pp. 76 290I–76 290I–12.
[3] S. Leung and J. Qian, "An adjoint-state method for three-dimensional transmission traveltime tomography using rst arrivals," Comm. in Math and Sci. 4(1), p. 2006, 249-266.
[4] J.A. Jensen, S.I. Nikolov, K.L. Gammelmark, M.H. Pedersen, Synthetic aperture ultrasound imaging, Ultrasonics 44 (2006) e5–e15.
[5] K. Wang, C. Huang, Y.J. Kao, C.Y. Chou, A.A. Oraevsky, M.A. Anastasio, "Accelerating image reconstruction in three-dimensional optoacoustic tomography on graphics processing units",Medical Physics, 40 (2) (2013), p. 023301.
[6] Amir Beck and Marc Teboulle, "A fast iterative shrinkage-thresholding algorithm for linear inverse problems," SIAM J. Img. Sci., 2(1):183–202, March 2009.

11. Appendices
1- Manuscript: "Waveform Inversion with Source Encoding for Breast Speed-of-Sound Reconstruction in Ultrasound Computed Tomography"
2- Abstract submitted for the poster presentation in SPIE Photonics West, 2014

3- Conference Proceedings, SPIE Photonics West, 2014
4- Abstract submitted for the poster presentation in SPIE Medical Imaging, 2014
5- Abstract submitted for the oral presentation in upcoming SPIE Photonics West, 2015
6- Co-author in the abstract submitted for the oral presentation in upcoming SPIE Medical Imaging, 2015

Investigation of a method for laser-induced ultrasound tomography that eliminates the need for ray-tracing

Fatima Anis, Yang Lou, Andre Conjusteau, Sergey Ermilov,
Alexander Oraevsky and Mark A. Anastasio*
Dept. of Biomedical Engineering, Washington University in St. Louis, 1 Brookings Dr.,
St. Louis, MO, USA 63130

*Corresponding author. Email: anastasio@seas.wustl.edu

ABSTRACT

In this work, we investigate a novel reconstruction method for laser-induced ultrasound tomography (UST) breast imaging that circumvents limitations of existing methods that rely on ray-tracing. There is currently great interest in developing hybrid imaging systems that combine optoacoustic tomography (OAT) and UST. There are two primary motivations for this: (1) the speed-of-sound (SOS) distribution reconstructed by UST can provide complementary diagnostic information; and (2) the reconstructed SOS distribution can be incorporated in the OAT reconstruction algorithm to improve OAT image quality. However, image reconstruction in UST remains challenging. The majority of existing approaches for UST breast imaging involve ray-tracing to establish the imaging operator. This process is cumbersome and can lead to severe inaccuracies in the reconstructed SOS images in the presence of multiple ray-paths and/or shadow zones.

To circumvent these problems, we implemented a partial differential equation-based Eulerian approach to UST that was proposed in the mathematics literature but never investigated for medical imaging applications. This method operates by directly inverting the Eikonal equation without ray-tracing. A numerical implementation of this method was developed and systematically compared to existing reconstruction methods for UST breast imaging. We demonstrated the ability of the new method to reconstruct accurate SOS maps from TOF data obtained by a 3D hybrid OAT/UST imager built by our team.

Investigation of the adjoint-state method for ultrasound computed tomography: A numerical and experimental study

Fatima Anis[a], Yang Lou[a], André Conjusteau[b],Richard Su[b], Tanmayi Oruganti[b], Sergey A. Ermilov[b], Alexander A. Oraevsky[b] and Mark A. Anastasio[a]

[a] Department of Biomedical Engineering, Washington University in St. Louis,
St. Louis, MO 63130 [b] TomoWave Laboratories, Inc., Houston TX

ABSTRACT

In this work, we investigate a novel reconstruction method for laser-induced ultrasound computed tomography (USCT) breast imaging that circumvents limitations of existing methods that rely on ray-tracing. There is currently great interest in developing hybrid imaging systems that combine optoacoustic tomography (OAT) and USCT. There are two primary motivations for this: (1) the speed-of-sound (SOS) distribution reconstructed by USCT can provide complementary diagnostic information; and (2) the reconstructed SOS distribution can be incorporated in the OAT reconstruction algorithm to improve OAT image quality. However, image reconstruction in USCT remains challenging. The majority of existing approaches for USCT breast imaging involve ray-tracing to establish the imaging operator. This process is cumbersome and can lead to inaccuracies in the reconstructed SOS images in the presence of multiple ray-paths and/or shadow zones. To circumvent these problems, we implemented a partial differential equation-based Eulerian approach to USCT that was proposed in the mathematics literature but never investigated for medical imaging applications. This method operates by directly inverting the Eikonal equation without ray-tracing. A numerical implementation of this method was developed and compared to existing reconstruction methods for USCT breast imaging. We demonstrated the ability of the new method to reconstruct SOS maps from TOF data obtained by a hybrid OAT/USCT imager built by our team.

Keywords: ultrasound tomography, optoacoustic tomography, photoacoustic tomography, breast cancer imaging

1. INTRODUCTION

Transmission ultrasound computed tomography (USCT) is an emerging imaging modality with many biomedical applications. USCT can be employed to retrieve anatomical information of tissues e. g. speed of sound, acoustical impedance and reflectivity. The effectiveness of USCT in tumor detection has been discussed in recent studies.[1–3] It is known that cancerous tissues have higher SOS values compared to the benign fatty masses and healthy breast tissues. A clinical ultrasound ring array scanner for breast cancer diagnosis (Computed Ultrasound Risk Evaluation (CURE)) has been proposed.[1,2] This system consists of 256 transducer elements distributed on a ring with a 20 cm diameter. Another prototype has also been developed by SoftVue and consists of 2048 transducers.[4] The system is capable of reconstructing a series of 2D slices of the SOS, acoustic attenuation, and reflectivity distributions. Techniscan (Salt Lake City UT) introduced a commercial USCT system that employs three transducer probes placed around the breast. The transducer system is mechanically rotated to reconstruct 2D slices and subsequently vertically scanned to capture multiple slices to obtain 3D images.[5] Finally, an ultrasound imaging module capable of generating three-dimensional SOS distributions has been investigated by researchers at the Karlsruhe Institute of Technology (KIT), Germany.[6]

Biomedical applications of USCT commonly employ geometrical acoustics models and require time-of-flight (TOF) measurements. TOF data that have been recorded for many source-receiver pairs can be employed for reconstruction of the SOS distribution. The reconstruction of the speed of sound distribution is conventionally performed by using ray-tracing (RT) methods.[1,2,7,8] To account for the curvature of the ray paths, the rays are

---

(Send correspondence to F. Anis)
Fatima Anis: E-mail: fatimaanis@seas.wustl.edu, Telephone: 1 314 935 9403

traced along the negative gradient of the TOF distribution.[8] Ray-tracing can become cumbersome, especially for three-dimensional USCT. Moreover, unlike X-ray computed tomography, the heterogeneous SOS distribution results in uneven ray-distributions, which makes the inverse problem ill-conditioned. In this work, we will investigate a different approach for SOS image reconstruction. This method, the adjoint state (AS) method, has previously been employed for seismic tomography.[9, 10] We are investigating the AS method for USCT for the first time for biomedical applications.

2. DESCRIPTION OF NUMERICAL STUDIES

To perform USCT using RT, we have employed the the geometrical ray theory for sound waves. This approximation results in a non-linear model, the eikonal equation, to relate the measured TOF values to the speed of sound distribution as

$$|\nabla T(\mathbf{r})| = \frac{1}{c(\mathbf{r})}. \tag{1}$$

In Eq. (1), ∇T is the gradient of the TOF, T, and c is the SOS distribution, both of which are a function of position as denoted by the position vector $\mathbf{r} \in \mathbb{R}^2$. Currently, the bent-ray reconstruction is a widely employed reconstruction technique for USCT because it incorporates refraction during sound wave propagation. The eikonal equation is solved numerically by finite difference methods[11] to obtain a TOF map for a given source corresponding to a certain speed of sound map $c(\mathbf{r})$.

2.1 Ray-tracing reconstruction method

In RT methods, the TOF is calculated as the line-integral over the slowness distribution over the ray-path connecting the source and the receiver location:

$$T(\mathbf{r}) = \int_{\Gamma(c)} \frac{1}{c(\mathbf{r})}. \tag{2}$$

The dependence of the ray-path, $\Gamma(c)$, on the SOS distribution makes it a non-linear problem. The discretized imaging model is given by

$$\mathbf{T} = \mathbf{H}(\mathbf{c})\frac{1}{\mathbf{c}}, \tag{3}$$

where $\mathbf{T}$ is a vector of TOF measurments, $\mathbf{c}$ is a finite-dimensional representation of the SOS, and $\mathbf{H}(\mathbf{c})$ is the system matrix. To formulate $\mathbf{H}(\mathbf{c})$, we implemented a RT method. Weights were assigned to pixels in the discrete SOS map based on the number of times each pixel was intersected by the rays. This weight matrix constitutes $\mathbf{H}(\mathbf{c})$.

To estimate the SOS distribution from the measured TOF data, we solved the following optimization problem:

$$\hat{\mathbf{c}} = \arg \min_{\mathbf{c}} \parallel \mathbf{T} - \mathbf{T}^* \parallel^2 + \nu g(\mathbf{c}), \tag{4}$$

where $\hat{\mathbf{c}}$ denotes the sought-after estimate of the the SOS distribution, $\mathbf{T}^*$ is the measured TOF data from all source-transducer pairs, $g(\mathbf{c})$ is a penalty function, ν is a regularization parameter, and $\mathbf{T}$ is the computed TOF found by solving (1). To minimize Eq. (4) we used the Limited BFGS method.[12] In solving the nonlinear optimization problem, we evaluated the gradient of Eq. (4) as

$$\nabla \mathbf{c} = 2\mathbf{H}(\mathbf{c})^T \left[\mathbf{H}(\mathbf{c})\mathbf{c} - \mathbf{T}^* \right] + \nu \nabla g(\mathbf{c}). \tag{5}$$

It should be noted from the above equation that the first term is a linear approximation of the true non-linear gradient of the objective function. The above linearized gradient is primarily used in USCT for biomedical applications.

2.2 Adjoint-state-based reconstruction method

We implemented a previously proposed algorithm for USCT reconstructed based on the adjoint-state method.[9] The mismatch energy functional between the measured and simulated data is defined as[9]

$$E[c(\mathbf{r})] = \frac{1}{2} \int_S |T(\mathbf{r}) - T^*(\mathbf{r})|^2 d\Omega, \tag{6}$$

where $T^*|_S$ is the measured TOF and $T|_S$ is computed by solving Eq. (1). The quantity in Eq. (6) — the energy functional — measures the L^2-difference between the the solution of the eikonal equation, T, and the experimental measurement, T^*, on the measurement surface S. Using the adjoint-state method for a small perturbation $\epsilon \tilde{c}$ to c, the gradient of the energy is defined:

$$\delta E = \epsilon \int_V \frac{\tilde{c}(\mathbf{r})\lambda(\mathbf{r})}{c^3(\mathbf{r})} d\Omega \tag{7}$$

Here, V is volume enclosed the measurement surface S and $\lambda(\mathbf{r})$ is the adjoint function to $T(\mathbf{r})$ that satisfies the following adjoint equation:

$$\nabla \cdot [\lambda(\mathbf{r})\nabla T(\mathbf{r})] = 0 \tag{8}$$

with the boundary condition,

$$[\mathbf{n} \cdot \nabla T(\mathbf{r})]\lambda(\mathbf{r})|_S = [T^*(\mathbf{r}) - T(\mathbf{r})]_S. \tag{9}$$

Here $\mathbf{n}$ is the unit outward normal of the surface S. To minimize the energy using the method of gradient descent, a perturbation $\tilde{c}(\mathbf{r}) = -\lambda(\mathbf{r})/c^3(\mathbf{r})$ is defined. This leads to

$$\delta E = -\epsilon \int_V \tilde{c}^2(\mathbf{r}) d\Omega \leq 0, \tag{10}$$

where V denotes the region interior to S. By solving Eqs. (8) and (9), the update, $\tilde{c}(\mathbf{r})$, to the SOS distribution can be computed. Specifically, the SOS distribution is updated at each step as:

$$c^{k+1} = c^k + \epsilon^k \tilde{c}^k \tag{11}$$

until a convergence criterion is reached. The following two conditions are required of the SOS distribution: (i) $\tilde{c}^k|_S = 0$ and (ii) c^{k+1} is smooth. To fulfill (ii), a regularization term similar to the one used in Eq. (4) was included. The filtering scheme defined in Lueng's work[9] was also implemeted. The step size, ϵ^k, can be determined by using the Armijo-Golstein rule or by simply setting $\epsilon^k = \epsilon$. The update scheme described in Eq. (11) takes a large number of iterations to converge. Therefore, we used the limited-memory Broydon-Fletcher Goldfarb-Shanno (L-BFGS) method to solve for this nonlinear optimization problem. We solved the adjoint-state equation (8) using the fast-sweeping method[9] with the boundary conditions defined in Eq. (9).

2.3 Experimental Setup

The experimental setup consists of a single laser ultrasound (LU) source and a 64 transducer elements arranged in an arc. The array aperture spans a 152 degree arc with a radius of 65 mm. The imaging module is mounted and centered on a rotational stage operated by a stepper motor, which is used to obtain TOF measurement for 150 views. The distance between the central element of the arc array and the LU source is 130 mm. Optoacoustic imaging was concurrently performed. More detail about the LU sources and the transducer array can be found elsewhere.[13, 14]
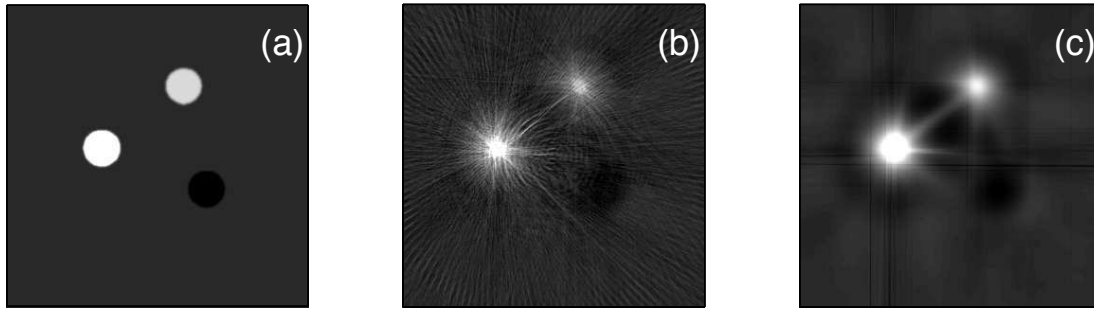
Figure 1. (a) Speed of sound distribution for the phantom; reconstructed SOS distribution for the RT method (b) and for the AS method (c).

3. RESULTS AND DISCUSSION

Computer-simulation studies were conducted to compare the RT method with the AS method. In this study, the objective function did not include a penalty and least squares estimates of the SOS distributions were computed. The two-dimensional phantom depicting the SOS distribution is shown in Figure 1(a). The phantom consists of three discs of 4.72 mm diameter with constant SOS of 1.48, 1.6 and 1.7 mm/μs, respectively. The pressure data were generated using the k-Wave software package[15] with a geometry and acoustic properties consistent with our experimental system design. Gaussian white noise was added to the calculated pressure signal to obtain experimentally-relevant SNRs. Figures 1(b) and 1(c) show the reconstructed SOS distribution for the RT method and the AS method, respectively. In the case of the RT method, streak artifacts are very visible as compared to the AS method. All three structures can be seen in the AS reconstruction of the SOS distribution. The results show that the AS method can be successfully used to perform USCT for biomedical applications.

To check the accuracy of the reconstructed SOS distribution, we selected 2 mm x 2mm regions at different locations and calculated the avaeraged SOS and standard deviation in those region. The location of the five regions is shown in Fig.2(a). The bar plot in Fig.2(b) shows the averaged SOS values for both the RT and AS method. It can be seen that AS gives accurate SOS values for the selected regions. The maximum standard deviation was 0.0226 mm/μs for region "A".

Finally, we studied the use of the AS method to perform SOS image reconstruction for the experimentally measured TOF from our LU system. The experimental phantom consists of three tubes each with a 4.72 mm internal diameter. Tubes were filled with water at different salt concentrations to induce different SOS values and $CuSO_4$ was added to provide optical contrast. For this case, concurrent optoacoustic (OA) and ultrasonic data acquisition was performed. The OA reconstruction of the phantom is shown in Fig. 3(a) and the SOS reconstruction is shown in Fig. 3(b). The SOS image was found via the AS reconstruction method. Once again, all three discs are visible in the reconstructed SOS distribution.
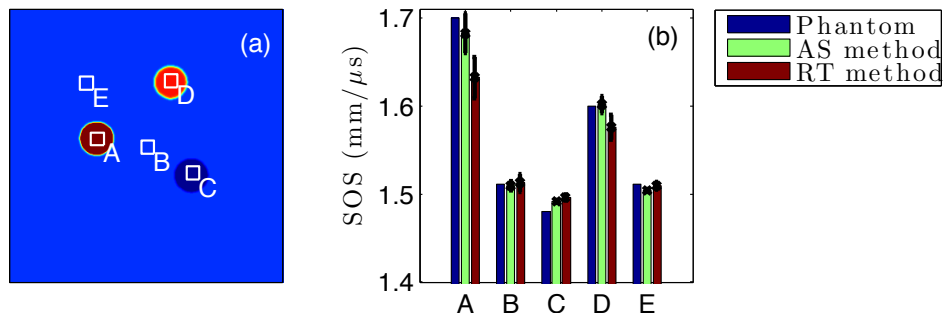

Figure 2. (a) Speed of sound distribution for the phantom with the marked location of five regions; (b) bar plot for the averaged SOS values in five regions for phantom, AS method, and RT method.
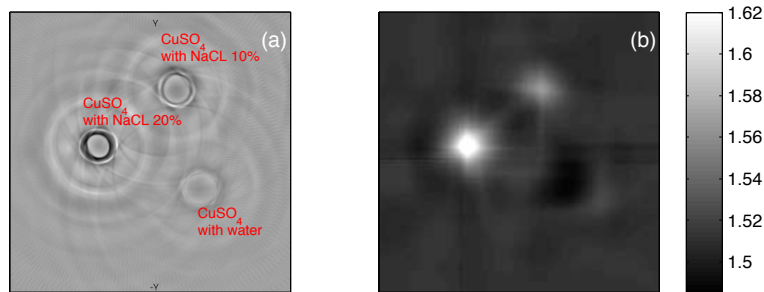
Figure 3. (a) Optoacoustic image of three tubes; (b) reconstructed SOS distribution using the AS method.

4. SUMMARY

The adjoint state method has been implemented for biomedical applications of USCT. Images reconstructed from both simulation studies and measured TOF data were presented. Ray tracing becomes much more cumbersome for three-dimensional USCT. Consequently, the adjoint state method holds great promise for that application. Further numerical studies will also be performed to quantify resolution and noise propagation in the adjoint state method.

ACKNOWLEDGMENTS

REFERENCES

1. N. Duric, P. Littrup, L. Poulo, A. Babkin, R. Pevzner, E. Holsapple, O. Rama, and C. Glide, "Detection of breast cancer with ultrasound tomography: First results with the computed ultrasound risk evaluation (cure) prototype," *Med. Phys.* **34**(2), pp. 773–785, 2007.

2. C. Li, N. Duric, P. Littrup, and L. Huang, "In vivo breast sound-speed imaging with ultrasound tomography," *Ultrasound Med. Biol.* **35**(10), pp. 1615 – 1628, 2009.

3. A. Leproux, M. van Beek, U. de Vries, M. Wasser, L. Bakker, O. Cuisenaire, M. van der Mark, and R. Entrekin, "Automated 3d whole-breast ultrasound imaging: results of a clinical pilot study," *Proc. SPIE* **7629**, pp. 762902–762902–10, 2010.

4. N. Duric, P. Littrup, S. Schmidt, C. Li, O. Roy, L. Bey-Knight, R. Janer, D. Kunz, X. Chen, J. Goll, A. Wallen, F. Zafar, V. Allada, E. West, I. Jovanovic, K. Li, and W. Greenway, "Breast imaging with the softvue imaging system: first results," *Proc. SPIE* **8675**, pp. 86750K–86750K–8, 2013.

5. J. Wiskin, D. Borup, S. Johnson, M. Berggren, D. Robinson, J. Smith, J. Chen, Y. Parisky, and J. Klock, "Inverse scattering and refraction corrected reflection for breast cancer imaging," **7629**, pp. 76290K–76290K–12, 2010.

6. R. Jiřík, I. Peterlik, N. Ruiter, J. Fousek, R. Dapp, M. Zapf, and J. Jan, "Sound-speed image reconstruction in sparse-aperture 3-d ultrasound transmission tomography," *Ultrasonics, Ferroelectrics and Frequency Control, IEEE Transactions on* **59**(2), pp. 254 –264, 2012.

7. J. Jose, R. G. H. Willemink, W. Steenbergen, C. H. Slump, T. G. van Leeuwen, and S. Manohar, "Speed-of-sound compensated photoacoustic tomography for accurate imaging," *Med. Phys.* **39**(12), pp. 7262–7271, 2012.

8. A. Hormati, I. Jovanović, O. Roy, and M. Vetterli, "Robust ultrasound travel-time tomography using the bent ray model," *Proc. SPIE* **7629**, pp. 76290I–76290I–12, 2010.

9. S. Leung and J. Qian, "An adjoint-state method for three-dimensional transmission traveltime tomography using rst arrivals," *Comm. in Math and Sci.* **4**(1), p. 2006, 249-266.

10. C. Taillandier, M. Noble, H. Chauris, and H. Calandra, "First-arrival traveltime tomography based on the adjoint-state method," *Geophysics* **74**(6), pp. WCB57–WCB66, 2009.
11. P. Podvin and I. Lecomote, "Finite difference computation of travel-times in very contrasted velocity model: A massively parallel approach and its associated tools," *Geophysical J. Int.* **105**, pp. 271–284, 1991.
12. R. H. Byrd, P. Lu, J. Nocedal, and C. Zhu, "A limited memory algorithm for bound constrained optimization," *SIAM J. Sci. Comput.* **36**, pp. 667–695, 199.
13. A. Conjusteau, V. V. Nadvoretskiy, S. A. Ermilov, and A. A. Oraevsky, "Generation of wide-directivity broadband ultrasound by short laser pulses," *Proc. SPIE* **8581**, pp. 85814U–85814U–8, 2013.
14. S. A. Ermilov, A. Conjusteau, T. Hernandez, R. Su, V. Nadvoretskiy, D. Tsyboulski, F. Anis, M. A. Anastasio, and A. A. Oraevsky, "3d laser optoacoustic ultrasonic imaging system for preclinical research," *Proc. SPIE* **8581**, pp. 85810N–85810N–5, 2013.
15. B. E. Treeby, J. Jaros, A. P. Rendell, and B. T. Cox, "Modeling nonlinear ultrasound propagation in heterogeneous media with power law absorption using a k-space pseudospectral method," *J. Acous. Soc. Am.* **131**(6), pp. 4324–4336, 2012.

Investigation of adjoint-state method for ultrasound tomography that eliminates the need for ray-tracing

Fatima Anis,Yang Lou,Mark A. Anastasio

Department of Biomedical Engineering
Washington University in St. Louis, St. Louis, MO USA

This work has not been submitted for presentation or publication elsewhere.

Abstract

Our work introduces an ultrasound tomography (UST) reconstruction algorithm based on the adjoint method for medical imaging. This method improves current ray-tracing based UST reconstruction algorithm and has been previously applied to seismic travel-time tomography [S. Leung and J. Qian, Comm. Math. Sci. **4** (2006)]. Ultrasound tomography has received wide attention for its ability to help breast cancer diagnosis both by providing speed of sound and attenuation information, as well as providing adjunct imaging data for optoacoustic tomography (OAT). Current image reconstruction algorithms for UST are usually based on ray-tracing and gradient methods. Our investigation shows two drawbacks of these methods that lead to inaccuracy in image reconstruction. First, ray bending in ray-tracing will cause an uneven distribution of ray paths. This will lead to insufficient updates in shadow zones (regions covered by few ray paths) and cause artifacts. While this effect can be compensated by regularization to some extent, we show that it cannot be avoided completely in ray-tracing methods. Second, often, a linear approximation of the gradient objective function is used, which also introduces errors into the gradient descent optimization method. We will demonstrate that using the adjoint method to directly compute the Frechet derivative of the continuous non-linear objective function can circumvent both drawbacks of the ray-tracing method. Numerical simulations are then given to show the improvement of our method over the ray-tracing method.

1. DESCRIPTION OF PURPOSE

Transmission ultrasound tomography (UST) is an emerging modality that has a spectrum of biomedical applications. The transmitted ultrasound signal carries anatomical information about the object, e. g. speed of sound, acoustical impedance and reflectivity. Biomedical applications of UST commonly employ geometrical acoustics models and require time-of-flight (TOF) measurements. TOF data that have been recorded for many source-receiver pairs can be employed for reconstruction of the speed-of-sound (SOS) distribution.

We will present a comparison of two different algorithms for the accuracy and efficiency to perform ultrasound computed tomography. One of the methods has widely been utilized for the medical applications of ultrasound tomography. In this ray-tracing method [Manohar, *et. al.*, Appl. Phys. Lett. 131911, 2007], the eikonal equation is solved and a system matrix is formulated using the ray paths traced from the receivers locations to the source locations. The other method, the adjoint -state method [S. Leung and J. Qian, Comm. Math. Sci. **4** (2006)], eliminates the need to calculate ray paths and the descent direction is calculated by solving the adjoint state equation.

(Send correspondence to Mark A. Anastasio)
Mark A. Anastasio: E-mail: anastasio@wustl.edu, Telephone: 1 314 935 3637

2. METHODS

To perform UST, we have used the the geometrical ray theory for the sound waves. This approximation results in a non-linear model, the eikonal equation, to relate the measured time of flight (TOF) values to the speed of sound distribution (SOS)

$$|\nabla T(\mathbf{r})| = \frac{1}{c(\mathbf{r})} \tag{1}$$

In Eq. (1), ∇T is the gradient of the travel time, T, and c is the SOS distribution, which both are a function of position as denoted by the position vector $\mathbf{r} \in \mathbb{R}^2$. Currently, the bent-ray reconstruction is a widely used reconstruction technique for UST because it incorporates refraction during sound wave propagation. The eikonal equation is solved by either the Fast Marching Method or a Finite Difference Method to obtain a time-of-flight map for a given source corresponding to a certain speed of sound map $c(\mathbf{r})$.

2.1 Ray-tracing-based reconstruction method

We write the optimization problem as:

$$\hat{\mathbf{c}} = \arg\min_{\mathbf{c}} \parallel \mathbf{T} - \mathbf{T}^* \parallel^2 + \nu g(\mathbf{c}), \tag{2}$$

where $\mathbf{c}$ is the discrete representation of the SOS distribution, $\hat{\mathbf{c}}$ is the estimate of the the SOS distribution, $\mathbf{T}^*$ is the TOF measurement of all transducer pairs, $g(\mathbf{c})$ is a regularization term dependent on the SOS, ν is a regularization parameter, and $\mathbf{T}$ is the computed TOF found by solving (1). Mathematically, $\mathbf{T}$ can be expressed as

$$\mathbf{T} = \mathbf{H}(\mathbf{c})\frac{1}{\mathbf{c}}, \tag{3}$$

where $\mathbf{H}(\mathbf{c})$ is the system matrix. To formulate $\mathbf{H}(\mathbf{c})$, we implemented the ray-tracing method between each receiver and source transducer pair. Weights were assigned to pixels in the discrete representation of the object based on the number of times each pixel was intersected by the rays. This weight matrix constitutes $\mathbf{H}(\mathbf{c})$. To minimize Eq. (2) we used the Limited BFGS method. In solving the nonlinear optimization problem, we evaluated the gradient of Eq. (2) as

$$\nabla \mathbf{c} = 2\mathbf{H}(\mathbf{c})^T (\mathbf{H}(\mathbf{c})\mathbf{c} - \mathbf{T}^*) + \nu \nabla g(\mathbf{c}). \tag{4}$$

It should be noted from the above equation that the first term is a linear approximation of the true non-linear gradient of the objective function. The above linearized gradient is primarily used in UST for the biomedical applications. It is impractical to numerically calculate the true gradient of Eq. (2).

2.2 Adjoint-state-based reconstruction method

We define the mismatch energy functional between measured and simulated data as [S. Leung and J. Qian, Comm. Math. Sci. **4** (2006)]

$$E[c(\mathbf{r})] = \frac{1}{2} \int_S |T(\mathbf{r}) - T^*(\mathbf{r})|^2 d\Omega, \tag{5}$$

where c is the speed of sound, $T^*|_S$ is the measurement, and $T|_S$ is computed by solving the eikonal equation, Eq. (1). The quantity in Eq. (5) — the energy functional — measures the L^2-difference between the the solution of the eikonal equation, T, and the experimental measurement, T^*, on the measurement surface S. Using the adjoint-state method for a small perturbation $\epsilon\tilde{c}$ to c, we define the gradient of the energy:

$$\delta E = \epsilon \int_S \frac{\tilde{c}(\mathbf{r})\lambda(\mathbf{r})}{c^3(\mathbf{r})} d\Omega \tag{6}$$

Here $\lambda(\mathbf{r})$ is the adjoint variable and satisfies the following adjoint equation:

$$\nabla \cdot [\lambda(\mathbf{r})\nabla T(\mathbf{r})] = 0 \tag{7}$$

with the boundary condition,

$$[\mathbf{n} \cdot \nabla T(\mathbf{r})]\lambda(\mathbf{r})|_S = [T^*(\mathbf{r}) - T(\mathbf{r})]_S. \tag{8}$$

Here $\mathbf{n}$ is the unit outward normal of the surface S. To minimize the energy using the method of gradient descent we choose the perturbation $\tilde{c}(\mathbf{r}) = -\lambda(\mathbf{r})/c^3(\mathbf{r})$. This leads to

$$\delta E = -\epsilon \int_S \tilde{c}^2(\mathbf{r})d\Omega \leq 0. \tag{9}$$

By solving Eqs. (7) and (8), the update $\tilde{c}(\mathbf{r})$ to the SOS distribution can be computed. Specifically, the SOS distribution is updated at each step by:

$$c^{k+1} = c^k + \epsilon^k \tilde{c}^k \tag{10}$$

until a convergence criterion is reached. The following two conditions are required of the SOS distribution: (i) $\tilde{c}^k|_S = 0$ and (ii) c^{k+1} is smooth. To fulfill (ii), a regularization term similar to the one used in Eq. (2) was included. The step size, ϵ^k, can be determined by using Armijo-Golstein rule or by simply setting $\epsilon^k = \epsilon$. The update scheme described in Eq. (10) takes a large number of iterations to converge. Therefore, we used the limited-memory Broydon-Fletcher Goldfarb-Shanno (L-BFGS) method to solve for this nonlinear optimization problem.

3. RESULTS

We performed image reconstruction simulations for two different numerical phantoms using a ray-tracing method. In one of these breast phantoms, the SOS value for the subcutaneous fat was chosen to be 1375 m/s and the background SOS value was fixed at 1480 m/s to model a large variation in the SOS distribution. In the second 2D breast phantom, SOS value for the subcutaneous fat was chosen to be 1475 m/s and the background SOS value was chosen to be1500 m/s to yield a sample with small contrast in the SOS distribution. We used 128 sources and 128 receivers and calculated the measured TOF data using the bent-ray method. In this case, if the output of Eq. (4) is close to the exact gradient of the objective function, it is expected to recontrust the original SOS distribution. The reconstructed image will be degraded for the larger variation in SOS distribution when the linearized approximation is used to calculate $\nabla(\mathbf{c})$ given in Eq. (4).

It can clearly be seen from the Fig. (1) that image quality is degraded when the contrast in the SOS distribution becomes larger. For high contrast situations, the reconstructed image is blurred and we cannot quantitatively recover the SOS distribution. In principle, both images will look like the numerical phantom if the gradient in Eq. (4) is evaluated accurately. We will present results from the adjoint-state to address this issue.

4. NEW BREAKTHROUGH WORK

Our formulation for the ray-tracing method and adjoint state method will be applied for the reconstruction of speed of sound distributions. Our focus is to compare these methods specifically for breast imaging. To achieve this, we implemented a numerical ring scanner geometry similar to [N. Duric *et. al.*, Med. Phys. **34**(2), 773 (2007)]. We will present the comparison for a numerical breast phantom comprised of a distribution of malignant, cystic, and fatty masses in the region of glandular tissue inside a ring of subcutaneous fat tissue. Moreover, we will also present the comparison study for a numerical phantom of SOS distribution synthesized from a slice through an MRI of a breast. The comparison between these method will be quantified by assessing the quality of images using some quantitative physical tests e.g. least-square error, resolution.
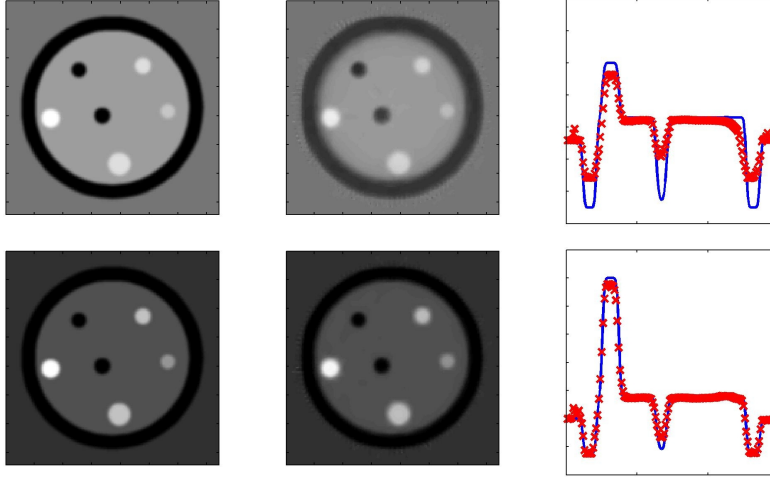
Figure 1: Comparison of the SOS image reconstruction for two different phantoms. The true phantoms are shown in the left column. The top phantom has a larger variation in the speed-of-sound values. The middle column of images shows the images reconstructed by use of the bent-ray model, with the corresponding image profiles displayed in the right column.

5. CONCLUSION

This study demonstrates the use of the adjoint-state method for ultrasound imaging. The ray-tracing method has primarily been used in ultrasound computed tomography, but is cumbersome and prevents the accurate calculation of the gradient of the cost function. By use of the adjoint method, the gradient is calculated accurately and improved reconstructions of an object's speed of sound distribution can be obtained.

Accelerated iterative image reconstruction in three-dimensional optoacoustic tomography

Fatima Anis[a], Yang Lou[a], Kun Wang[a], Richard Su[a], Andre Conjusteau[b], Sergey Ermilov[b], Alexander A. Oraevsky[b] and Mark A. Anastasio[a]*

[a] Department of Biomedical Engineering, Washington University in St. Louis, 1 Brookings Dr., St. Louis, Missouri 63130
[b] TomoWave Laboratories, Houston, Texas 77081

*Corresponding author. Email: anastasio@seas.wustl.edu

ABSTRACT

Optoacoustic tomography (OAT), also known as photoacoustic computed tomography, has found many biomedical applications. Because they can model complicated imaging physics, compensate for imperfect data acquisition systems, and exploit prior information regarding the object, iterative image reconstruction algorithms, in general, produce higher quality images than do analytical image reconstruction algorithms. However, three-dimensional (3D) iterative image reconstruction is computationally burdensome. Even with graphics processing unit (GPU)-accelerated implementations, to our knowledge, it still takes at least five hours to reconstruct the 3D volume of a whole-body mouse. This computational burden greatly hinders the application of advanced image reconstruction algorithms to applications with a large field-of-view (FOV), such as breast imaging.

In this study, an improved GPU-based implementation of a numerical imaging model and its adjoint have been developed for use with general gradient-based iterative image reconstruction algorithms. Particularly, two types of computation-reduced discretization methods are employed; a parallel fast Fourier transform (FFT) algorithm is employed to accelerate the calculation of the temporal convolution with ultrasonic transducer responses; and a volume-reduction method is proposed to reduce the computation for applications with irregular FOV. Both computer-simulation and experimental studies are conducted to investigate the efficiency and accuracy of the proposed implementation. The results suggest that the proposed implementation is more than **five** times faster than previous implementations. Using the proposed implementation, a 3D whole-body mouse image can be reconstructed in less than one hour. The developed

algorithm is also evaluated for 3D OAT breast imaging with sub millimeter resolution.

Breast Ultrasound computed tomography using waveform inversion with source encoding

Kun Wang [a], Thomas Matthews [a], Fatima Anis, [a] Cuiping Li[b], Neb Duric[b,c], and Mark A. Anastasio[a]

[a] Department of Biomedical Engineering, Washington University in St. Louis,
St. Louis, MO 63130
[b] Delphinus Medical Technologies, Plymouth MI 48170
[c] Karmanos Cancer Inistitute, Wayne State University, Detroit MI 48201

ABSTRACT

Ultrasound computed tomography (USCT) holds great promise for improving the detection and management of breast cancer. Because they are based on the acoustic wave equation, waveform inversion-based reconstruction methods can produce images that possess improved spatial resolution properties over those produced by ray-based methods. However, waveform inversion methods are computationally demanding and have not been applied widely in USCT breast imaging. A computationally efficient numerical wave equation solver has been reported based on a modified Fresnel propagation, which only applies to USCT systems with a planar incident wave. For breast imaging systems with a spherical incident wave, waveform inversion-based reconstruction methods remain computationally challenging.

In this work, source encoding concepts are employed to develop an accelerated USCT reconstruction method that circumvents the large computational burden of conventional waveform inversion methods. This method, referred to as the waveform inversion with source encoding (WISE) method, encodes the measurement data using a random encoding vector and determines an estimate of the speed-of-sound distribution by solving a stochastic optimization problem by use of a stochastic gradient descent algorithm. For practical applications, a data-filling strategy is proposed to mitigate source inferences to its neighbor receivers. Computer-simulation and experimental phantom studies are conducted to demonstrate the use of the WISE method. Using a single graphics processing unit card, each iteration can be completed within 25 seconds for a 128×128 mm^2 reconstruction region. The results suggest that the WISE method maintains the high spatial resolution of waveform inversion methods while significantly reducing the computational burden.

1. PURPOSE

This study is focused on the image reconstruction of breast speed-of-sound (SOS) distribution in USCT. The majority of USCT image reconstruction methods for breast imaging investigated to date have been based on approximations to the acoustic wave equation.[1,2] A relatively popular class of methods is based on geometrical acoustics. They are commonly referred to as 'ray-based' methods. Although ray-based methods can be computationally efficient, the spatial resoultion of the images they produce is limited due to the fact that diffraction effects are not modelled.[3,4] This is undesirable for breast imaging applications, in which the ability to resolve fine features, e.g., tumor spiculations, is important for distinguishing healthy from diseased tissues.

USCT reconstruction methods based on the acoustic wave equation, also known as full-wave inverse scattering or waveform inversion methods, have also been explored for a variety of applications including medical imaging.[4–7] Because they account for higher-order diffraction effects, waveform inversion methods can produce images that possess higher spatial resolution properties than those produced by ray-based methods.[4,5] However, conventional waveform inversion methods are iterative in nature and require the wave equation to be solved numerically a large number of times at each iteration. Consequently, such methods can be extremely computationally burdensome. For special geometries,[7] efficient numerical wave equation solvers have been reported. However, apart from

---

special cases, the large computational burden of waveform inversion methods has hindered their widespread application.

The purpose of this study is to develop an algorithmically accelerated waveform inversion method for breast SOS reconstruction. Aided by a graphics processing unit (GPU)-accelerated implementation, the developed method will maintain the high spatial resolution of standard waveform inversion methods with a signifcant reduction in computational time.

2. METHODS

A conventional waveform inversion method seeks the solution of

$$\hat{\mathbf{c}} = \arg \min_{\mathbf{c}} \frac{1}{2} \sum_{m=0}^{M-1} \|\underline{\mathbf{g}}_m - \mathbf{H}^c \mathbf{s}_m\|^2 + \beta \mathcal{R}(\mathbf{c}), \tag{1}$$

where $\mathbf{c}$ is the sought-after object to be reconstructed, i.e, SOS distribution, $\underline{\mathbf{g}}_m$ denotes the measured data vector, $\mathbf{s}_m$ denotes the (known) source vector, $\mathbf{H}^c$ denotes a numerical wave equation solver (NWES) that maps the known source vector to the measured data vector, and $\mathcal{R}(\mathbf{c})$ and β denote the penalty term and the regularization parameter respectively. The superscript in $\mathbf{H}^c$ indicates the dependence of $\mathbf{H}^c$ on $\mathbf{c}$. Note that one USCT measurement involves firing a sequence of acoustic pulses in turn and recording the data corresponding to every pulse. Each pulse-firing and data recording process will be indexed by m for $m = 0, 1, \cdots, M - 1$. Solving Eqn. (1), in general, requires the calculation of $\frac{1}{2} \sum_{m=0}^{M-1} \nabla_c \|\underline{\mathbf{g}}_m - \mathbf{H}^c \mathbf{s}_m\|^2$, where ∇_c denotes the gradient operator with respect to $\mathbf{c}$. The gradient in each summand is commonly computed by use of an adjoint state method,[5] which requires two runs of the NWES. Repeating the gradient calculation for all sources results in $2M$ runs of the NWES at each iteration. This computational burden largely hinders the application of the conventional waveform inversion methods in practice.

In this study, a waveform inversion with source encoding (WISE) method was developed. The WISE method employs the objective function

$$\hat{\mathbf{c}} = \arg \min_{\mathbf{c}} \mathbf{E}_{\mathbf{w}} \left\{ \frac{1}{2} \|\underline{\mathbf{g}}^w - \mathbf{H}^c \mathbf{s}^w\|^2 \right\} + \beta \mathcal{R}(\mathbf{c}), \tag{2}$$

where $\mathbf{E}_{\mathbf{w}}$ denotes the expectation operator with respect to the random source encoding vector $\mathbf{w} \in \mathbb{R}^M$, and $\underline{\mathbf{g}}^w$ and $\mathbf{s}^w$ denote the $\mathbf{w}$-encoded data and source vectors, defined as

$$\underline{\mathbf{g}}^w = \sum_{m=0}^{M-1} [\mathbf{w}]_m \underline{\mathbf{g}}_m, \quad \text{and} \quad \mathbf{s}^w = \sum_{m=0}^{M-1} [\mathbf{w}]_m \mathbf{s}_m, \tag{3}$$

respectively. Equation (2) was solved by use of a stochastic gradient descent algorithm.[8] Because the stochastic gradient descent algorithm calculated the gradient of only one realization of the random variable $\frac{1}{2} \|\underline{\mathbf{g}}^w - \mathbf{M} \mathbf{H}^c \mathbf{s}^w\|^2$ at each iteration, the required number of NWES runs per iteration was reduced from $2M$ to 2. Although it, in general, requires more algorithm iterations to average out the randomness in the realizations, the WISE method, as demonstrated later, can greatly reduce the overall number of NWES runs. Both computer-simulation and experimental phantom studies were conducted to demonstrate the use of the WISE method for breast SOS reconstruction.

3. RESULTS

The images reconstructed from the computer-simulated noise-free data by use of the WISE method after 199 iterations and sequential waveform inversion method after 43 iterations are shown in Fig. 1-(a) and (b). As expected,[4,9] both images are more accurate and possess higher spatial resolution than the one reconstructed by use of the bent-ray reconstruction algorithm displayed in Fig. 1-(c). The images shown in Fig. 1-(a) and -(b) possess similar accuracies as measured by their Euclidean distances from the SOS phantom vector $\mathbf{c}$, namely 0.07% of $\|\mathbf{c}\|$ for the former and 0.08% of $\|\mathbf{c}\|$ for the latter. However, the reconstruction of Fig. 1-(a) required

only about 1.7% of the computational time required to reconstruct Fig. 1-(b), namely, 1.4 hours for the former and 81.4 hours for the latter respectively. This is because the WISE method required only 1018 NWES runs, which is signficantly less than the 58880 NWES runs required by the sequential waveform inversion method. With a similar number of NWES runs, (e.g., 1024), one can only complete a single algorithm iteration by use of the sequential waveform inversion method. The corresponding image, shown in Fig. 1-(d), lacks quantitative accuracy as well as qualitative value for identifying features. The results suggest that the WISE method maintains the advantages of the sequential waveform inversion method while significantly reducing the computational time.
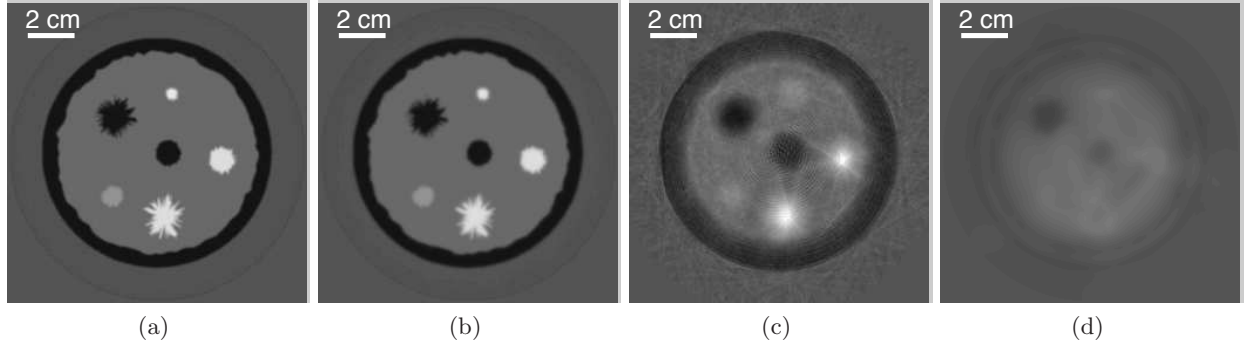

Figure 1. Images reconstructed by use of (a) the WISE method after the 199-th iteration $(1,018$ runs of NWES) (b) the sequential waveform inversion algorithm after the 43-rd iteration $(58,880$ runs of the NWES), (c) the bent-ray model-based SOS reconstruction method, and (d) the sequential waveform inversion algorithm after the 1-st iteration $(1,024$ runs of the NWES) from the noise-free non-attenuated data. The grayscale window is $[1.46, 1.58]$ mm/μs.

The images reconstructed from the experimentally-measured data are shown in Fig. 2. The spatial resolution of the image reconstructed by use of the WISE method is significantly higher than that reconstructed by use of the bent-ray model-based method. In particular, the structures labeled 'A' and 'B' possess clearly-defined boundaries. In addition, the structure labeled 'Cancer' in Fig. 2-(a) is almost indistinguishable in the image reconstructed by use of the bent-ray model-based method (see Fig. 2-(b)). The improved spatial resolution is expected because the WISE method takes into account the high-order diffraction effects, which are ignored by the bent-ray method.[4]
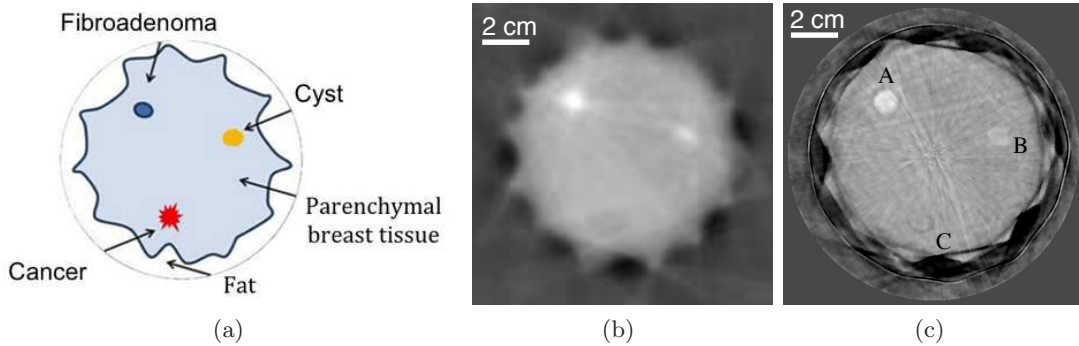

Figure 2. (a) Schematic of the breast phantom employed in the experimental study. Images reconstructed from the experimentally measured phantom data by use of (a) the bent-ray model-based SOS reconstruction method and (b) the WISE method after the 200-th iteration. The grayscale window is $[1.49, 1.57]$ mm/μs.

4. NEW OR BREAKTHROUGH WORK TO BE PRESENTED

Source encoding concepts are demonstrated in breast USCT experimental studies for the first time. Unlike previously studied waveform inversion methods that were based on the Helmholtz equation, the WISE method

is formulated by use of the time-domain acoustic wave equation. A GPU-accelerated NWES is developed that can compute 1800 time samples, on a 1024×1024 spatial grid, in 5 seconds. In addition, a data-filling strategy is proposed to mitigate the inference of the source with its neighboring receivers for practical applications.

5. CONCLUSION

It is known that waveform inversion-based reconstruction methods can produce SOS images that possess improved spatial resolution properties over those produced by ray-based methods. However, waveform inversion methods are computationally demanding and have not been applied widely in USCT breast imaging. In this work, based on the time-domain wave equation and motivated by recent mathematical results in the geophysics literature, the WISE method was developed that circumvents the large computational burden of conventional waveform inversion methods. This method encodes the measurement data using a random encoding vector and determines an estimate of the speed-of-sound distribution by solving a stochastic optimization problem by use of a stochastic gradient descent algorithm. With our current GPU-based implementation, the computation time was reduced from weeks to hours. The WISE method was systematically investigated in computer-simulation and experimental studies involving a breast phantom. The results suggest that the method holds value for USCT breast imaging applications in a practical setting.

6. DISCLOSURE

This work is original. Parts of this work have been submitted to *IEEE Transactions on Ultrasounics, Ferroelectrics and Frequency Control* and are under review.

REFERENCES

1. Kak, A. C. and Slaney, M., [*Principles of Computerized Tomographic Imaging*], IEEE Press (1988).
2. Huthwaite, P., Simonetti, F., and Duric, N., "Combining time of flight and diffraction tomography for high resolution breast imaging: Initial invivo results (l)," *The Journal of the Acoustical Society of America* **132**(3), 1249–1252 (2012).
3. Bates, R., Smith, V., and Murch, R., "Manageable multidimensional inverse scattering theory," *Phys. Rep.* **201**(4), 185 – 277 (1991).
4. Pratt, R. G., Huang, L., Duric, N., and Littrup, P., "Sound-speed and attenuation imaging of breast tissue using waveform tomography of transmission ultrasound data," in [*Proc. SPIE*], **6510**, 65104S–65104S–12 (2007).
5. Roy, O., Jovanović, I., Hormati, A., Parhizkar, R., and Vetterli, M., "Sound speed estimation using wave-based ultrasound tomography: theory and GPU implementation," in [*SPIE Medical Imaging*], 76290J–76290J, International Society for Optics and Photonics (2010).
6. Zhang, Z., Huang, L., and Lin, Y., "Efficient implementation of ultrasound waveform tomography using source encoding," in [*SPIE Medical Imaging*], 832003–832003, International Society for Optics and Photonics (2012).
7. Wiskin, J., Borup, D. T., Johnson, S. A., and Berggren, M., "Non-linear inverse scattering: High resolution quantitative breast tissue tomography," *The Journal of the Acoustical Society of America* **131**(5), 3802–3813 (2012).
8. Bousquet, O. and Bottou, L., "The tradeoffs of large scale learning," in [*Advances in Neural Information Processing Systems 20*], Platt, J., Koller, D., Singer, Y., and Roweis, S., eds., 161–168, Curran Associates, Inc. (2008).
9. Li, C., Sandhu, G. S., Roy, O., Duric, N., Allada, V., and Schmidt, S., "Toward a practical ultrasound waveform tomography algorithm for improving breast imaging," in [*Proc. SPIE*], **9040**, 90401P–90401P–10 (2014).

Waveform Inversion with Source Encoding for Breast Sound Speed Reconstruction in Ultrasound Computed Tomography

Kun Wang, *Member, IEEE,* Thomas Matthews, *Student Member, IEEE,*

Fatima Anis, Cuiping Li, Neb Duric,

and Mark A. Anastasio, *Senior Member, IEEE*

Abstract

Ultrasound computed tomography (USCT) holds great promise for improving the detection and management of breast cancer. Because they are based on the acoustic wave equation, waveform inversion-based reconstruction methods can produce images that possess improved spatial resolution properties over those produced by ray-based methods. However, waveform inversion methods are computationally demanding and have not been applied widely in USCT breast imaging. In this work, source encoding concepts are employed to develop an accelerated USCT reconstruction method that circumvents the large computational burden of conventional waveform inversion methods. This method, referred to as the waveform inversion with source encoding (WISE) method, encodes the measurement data using a random encoding vector and determines an estimate of the sound speed distribution by solving a stochastic optimization problem by use of a stochastic gradient descent algorithm. Both computer-simulation and experimental phantom studies are conducted to demonstrate the use of the WISE method. The results suggest that the WISE method maintains the high spatial resolution of waveform inversion methods while significantly reducing the computational burden.

Index Terms

K. Wang, T.P. Matthews, F. Anis, and M.A. Anastasio are with the Department of Biomedical Engineering, Washington University in St. Louis, St. Louis, MO 63130, e-mail: anastasio@wustl.edu

C. Li and N. Duric are with Delphinus Medical Technologies, Plymouth, MI 48170

N. Duric is also with Karmanos Cancer Institute, Wayne State University, 4100 John R. Street, 5 HWCRC, Detroit, MI 48201

Ultrasound computed tomography, Breast imaging, Waveform inversion, Source encoding, Sound-speed imaging

I. INTRODUCTION

After decades of research [1]–[4], advancements in hardware and computing technologies are now facilitating the clinical translation of ultrasound computed tomography (USCT) for breast imaging applications [5]–[9]. USCT holds great potential for improving the detection and management of breast cancer since it provides novel acoustic tissue contrasts, is radiation- and breast-compression-free, and is relatively inexpensive. [10], [11]. Several studies have reported the feasibility of USCT for characterizing breast tissues [4]–[7], [11], [12]. Although some USCT systems are capable of generating three images that depict the breast's acoustic reflectivity, acoustic attenuation, and sound speed distributions, this study will focus on the reconstruction of the sound speed distribution.

A variety of USCT imaging systems have been developed for breast sound speed imaging [6], [8], [11], [13]–[16]. In a typical USCT experiment, acoustic pulses that are generated by different transducers are employed, in turn, to insonify the breast. The resulting wavefieled data are measured by an array of ultrasonic transducers that are located outside of the breast. Here and throughout the manuscript, a transducer that produces an acoustic pulse will be referred to as an emitter; the transducers that receive the resulting wavefield data will be referred to as receivers. From the collection of recorded wavefield data, an image reconstruction method is utilized to estimate the sound speed distribution within the breast [6], [8], [11].

The majority of USCT image reconstruction methods for breast imaging investigated to date have been based on approximations to the acoustic wave equation [13], [17]–[24]. A relatively popular class of methods is based on geometrical acoustics, and are commonly referred to as 'ray-based' methods. These methods involve two steps. First, time-of-flight (TOF) data corresponding to each emitter-receiver pair are estimated [25]. Under a geometrical acoustics approximation, the TOF data are related to the sound speed distribution via an integral geometry, or ray-based, imaging model [17], [26]. Second, by use of the measured TOF data and the ray-based imaging model, a reconstruction algorithm is employed to estimate the sound speed distribution. Although ray-based methods can be computationally efficient, the spatial resoultion of the images they produce is limited due to the fact that diffraction effects are not modelled [23], [27]. This is

undesirable for breast imaging applications, in which the ability to resolve fine features, e.g., tumor spiculations, is important for distinguishing healthy from diseases tissues.

USCT reconstruction methods based on the acoustic wave equation, also known as full-wave inverse scattering or waveform inversion methods, have also been explored for a variety of applications including medical imaging [13], [22], [23], [28] and geophysics [29]–[31]. Because they account for higher-order diffraction effects, waveform inversion methods can produce images that possess higher spatial resolution than those produced by ray-based methods [23], [28]. However, conventional waveform inversion methods are iterative in nature and require the wave equation to be solved numerically a large number of times at each iteration. Consequently, such methods can be extremely computationally burdensome. For special geometries [13], [32], efficient numerical wave equation solvers have been reported. However, apart from special cases, the large computational burden of waveform inversion methods has hindered their widespread application.

A natural way to reduce the computational complexity of the reconstruction problem is to reformulate it in a way that permits a reduction in the number of times the wave equation needs to be solved. In the geophysics literature, source encoding methods have been proposed to achieve this [29]–[31]. When source encoding is employed, at each iteration of a prescribed reconstruction algorithm, all of the acoustic sources produced by the emitters are combined (or 'encoded') by use of a random encoding vector; So are the measured wavefield data. As a result, the wave equation may need to be solved as few as twice at each algorithm iteration. In conventional waveform inversion methods, this number would be equal to twice the number of emitters employed. Although conventional waveform inversion methods may require fewer algorithm iterations to obtain a specified image accuracy compared to source encoded methods, as demonstrated later, the latter can greatly reduce the overall number of times the wave equation needs to be solved.

In this study, a waveform inversion with source encoding (WISE) method for USCT sound speed reconstruction is developed and investigated for breast imaging with a circular transducer array. The WISE method determines an estimate of the SOS distribution by solving a stochastic optimization problem by use of a stochastic gradient descent algorithm [30], [33]. Unlike previously studied waveform inversion methods that were based on the Helmholtz equation [22], [23], the WISE method is formulated by use of the time-domain acoustic wave equation [34]–[36]

and utilizes broad-band measurements. The wave equation is solved by use of a computationally efficient k-space numerical wave equation solver that is accelerated using graphics processing units (GPUs). In order to mitigate the interference of the emitter on its neighboring receivers, a heuristic data replacement strategy is proposed. The method is validated in computer-simulation studies that include modelling errors and other physical factors. The practical applicability of the method is further demonstrated in studies involving experimental breast phantom data.

The remainder of the paper is organized as follows. In Section II, USCT imaging models in their continuous and discrete forms are reviewed. A conventional waveform inversion method and the WISE method for sound speed reconstruction are formulated in Section III. The computer-simulation studies and corresponding numerical results are presented in Sections IV and V, respectively. In Section VI, the WISE method is further validated in experimental breast phantom studies. Finally, the paper concludes with a discussion in Section VII.

II. BACKGROUND: USCT IMAGING MODELS

In this section, imaging models that provide the basis for image reconstruction in waveform inversion-based USCT are reviewed in their continuous and discrete forms.

A. USCT imaging model in its continuous form

Although a digital imaging system is properly described as a continuous-to-discrete (C-D) maping (See Chapter 7 in [37]), for simplicity, a USCT imaging system is initially described in its continuous form below.

In USCT breast imaging, a sequence of acoustic pulses is transmitted through the breast. We denote each acoustic pulse by $s_m(\mathbf{r}, t) \in \mathbb{L}^2(\mathbb{R}^3 \times [0, \infty))$, where each pulse is indexed by an integer m for $m = 0, 1, \cdots, M-1$ with M denoting the total number of acoustic pulses. Although it is spatially localized at the emitter location, each source can be expressed as a function of space and time. When the m-th pulse propagates through the breast, it generates a pressure wavefield distribution denoted by $p_m(\mathbf{r}, t) \in \mathbb{L}^2(\mathbb{R}^3 \times [0, \infty))$. If acoustic absorption and mass density variations are negligible, $p_m(\mathbf{r}, t)$ in an unbounded medium satisfies the acoustic wave equation [38]:

$$\nabla^2 p_m(\mathbf{r}, t) - \frac{1}{c^2(\mathbf{r})} \frac{\partial^2}{\partial t^2} p_m(\mathbf{r}, t) = -4\pi s_m(\mathbf{r}, t), \tag{1}$$

where $c(\mathbf{r})$ is the sought-after sound speed distribution. Equation (1) can be expressed in operator form as

$$p_m(\mathbf{r}, t) = \mathcal{H}^c s_m(\mathbf{r}, t), \tag{2}$$

where the linear operator $\mathcal{H}^c : \mathbb{L}^2(\mathbb{R}^3 \times [0, \infty)) \mapsto \mathbb{L}^2(\mathbb{R}^3 \times [0, \infty))$ denotes the action of the wave equation and is independent of the index of m. The superscript 'c' indicates the dependence of $\mathcal{H}^c$ on $c(\mathbf{r})$.

Consider that $p_m(\mathbf{r}, t)$ is recorded outside of the object for $\mathbf{r} \in \Omega_m$ and $t \in [0, T]$, where $\Omega_m \subset \mathbb{R}^3$ denotes a continuous measurement aperture. In this case, when discrete sampling effects are not considered, the USCT imaging model can be described as a continuous-to-continuous (C-C) mapping as:

$$g_m(\mathbf{r}, t) = \mathcal{M}_m \mathcal{H}^c s_m(\mathbf{r}, t), \quad \text{for} \quad m = 0, 1, \cdots, M - 1, \tag{3}$$

where $g_m(\mathbf{r}, t) \in \mathbb{L}^2(\Omega_m \times [0, T])$ denotes the measured data function, and the operator $\mathcal{M}_m$ is the restriction of $\mathcal{H}^c$ to $\Omega_m \times [0, T]$. Introducing the m-dependent operator $\mathcal{M}_m$ allows Eqn. (3) to describe USCT imaging systems in which the measurement aperture can vary with emitter location. Here and throughout the manuscript, we will refer to the process of firing one acoustic pulse and acquiring the corresponding wavefield data as one data acquisition indexed by m. The USCT reconstruction problem in its continuous form is to estimate the sound speed distribution $c(\mathbf{r})$ by use of Eqn. (3) and the data functions $\{g_m(\mathbf{r}, t)\}_{m=0}^{M-1}$.

B. USCT imaging model in its discrete forms

A digital imaging system is accurately described by a continuous-to-discrete (C-D) imaging model, which is typically approximated in practice by a discrete-to-discrete (D-D) imaging model to facilitate the application of iterative image reconstruction algorithms. A C-D description of the USCT imaging system is provided in Appendix A. Below, a D-D imaging model for waveform inversion-based sound speed reconstruction in USCT are presented. The D-D imaging model will be employed subsequently in the development of the WISE method in Section III.

Construction of a D-D USCT imaging model requires the introduction of a finite-dimensional approximate representations of the functions $c(\mathbf{r})$ and $s_m(\mathbf{r}, t)$, which will be denoted by the vectors $\mathbf{c} \in \mathbb{R}^N$ and $\mathbf{s}_m \in \mathbb{R}^{NL}$. Here, N and L denote the numbers of spatial and time samples employed for wave propagation calculation respectively. In waveform-based USCT, the way in

which $c(\mathbf{r})$ and $s_m(\mathbf{r}, t)$ are discretized to form $\mathbf{c}$ and $\mathbf{s}_m$ is dictated by the numerical method employed to solve the acoustic wave equation, referred to as a numerical solver. In this study, we employ a numerical solver based on a pseudospectral k-space method [34]–[36]. Accordingly, $c(\mathbf{r})$ and $s_m(\mathbf{r}, t)$ are sampled on Cartesian grid points as

$$[\mathbf{c}]_n = c(\mathbf{r}_n), \quad \text{and} \quad [\mathbf{s}_m]_{nL+l} = s_m(\mathbf{r}_n, l\Delta^t), \quad \text{for} \quad \begin{smallmatrix} n=0,1,\cdots,N-1 \\ l=0,1,\cdots,L-1 \end{smallmatrix}, \tag{4}$$

where Δ^t denotes the temporal sampling interval and $\mathbf{r}_n$ denotes the location of the n-th point.

For a given $\mathbf{c}$ and $\mathbf{s}_m$, the pseudospectral numerical solver can be described in operator form as

$$\mathbf{p}_m^{\mathrm{a}} = \mathbf{H}^{\mathrm{c}} \mathbf{s}_m, \tag{5}$$

where the matrix $\mathbf{H}^{\mathrm{c}}$ is of dimension $NL \times NL$ and represents a discrete approximation of the wave operator $\mathcal{H}^{\mathrm{c}}$ defined in Eqn. (2), and the vector $\mathbf{p}_m^{\mathrm{a}}$ represents the estimated pressure data at the grid point locations and has the same dimension as $\mathbf{s}_m$. The superscript 'a' indicates that these values are approximate, i.e., $[\mathbf{p}_m^{\mathrm{a}}]_{nL+l} \approx p_m(\mathbf{r}_n, l\Delta^t)$. We refer the readers to [34]–[36] for additional details regarding the pseudospectral numerical solver.

Because the pseudospectral numerical solver yields pressure data distributed over the whole Cartesian grid, a sampling matrix $\mathbf{M}_m$ is introduced to model the USCT data acquisition process as

$$\mathbf{g}_m^{\mathrm{a}} = \mathbf{M}_m \mathbf{p}_m^{\mathrm{a}} \equiv \mathbf{M}_m \mathbf{H}^{\mathrm{c}} \mathbf{s}_m, \tag{6}$$

where the $N^{\mathrm{rec}}L \times NL$ sampling matrix $\mathbf{M}_m$ extracts the pressure data corresponding to the receiver locations on the measurement aperture Ω_m with N^{rec} denoting the number of receivers, and $\mathbf{g}_m^{\mathrm{a}}$ is the predicted data vector that approximates the true measurements. When the receiver and grid point locations do not coincide, interpolation methods are required. As an example, when a nearest-neighbor interpolation method is employed, the elements of $\mathbf{M}_m$ are defined as

$$[\mathbf{M}_m]_{n^{\mathrm{rec}}L+l, nL+l} = \begin{cases} 1, & \text{for} \quad n = \mathcal{I}_m(n^{\mathrm{rec}}), \\ 0, & \text{otherwise}, \end{cases} \tag{7}$$

where $[\mathbf{M}_m]_{n^{\mathrm{rec}}L+l, nL+l}$ denotes the element of $\mathbf{M}_m$ at the $(n^{\mathrm{rec}}L+l)$-th row and the $(nL+l)$-th column, and $\mathcal{I}_m(n^{\mathrm{rec}})$ denotes the index of the grid point that is closest to $\mathbf{r}(m, n^{\mathrm{rec}})$. Here, $\mathbf{r}(m, n^{\mathrm{rec}})$ denotes the location of the n^{rec}-th receiver at the m-th data acquisition. In summary, Eqn. (6) represents the D-D imaging model that will be employed in the remainder of this study.

Note that because of the dependence of $\mathbf{M}_m$ on m, a varying detection geometry among data acquisitions can be described by use of this model.

III. WAVEFORM INVERSION WITH SOURCE ENCODING FOR USCT

A. Sequential waveform inversion in its discrete form

A conventional waveform inversion method that does not utilize source encoding will be employed as a reference for the developed WISE method and is briefly described below. Like other conventional approaches, this method sequentially processes the data acquisitions $\mathbf{g}_m$ for $m = 0, 1, \cdots, M-1$ at each iteration of the associated algorithm. As such, we will refer to the conventional method as a sequential waveform inversion method.

A sequential waveform inversion method can be formulated as a non-linear numerical optimization problem:

$$\hat{\mathbf{c}} = \arg\min_{\mathbf{c}}\{\mathcal{F}(\mathbf{c}) + \beta\mathcal{R}(\mathbf{c})\}, \tag{8}$$

where $\mathcal{F}(\mathbf{c})$, $\mathcal{R}(\mathbf{c})$, and β denote the data fidelity term, the penalty term, and the regularization parameter, respectively. The data fidelty term $\mathcal{F}(\mathbf{c})$ is defined as a sum of squared ℓ^2-norms of the data residuals corresponding to all data acquisitions as:

$$\mathcal{F}(\mathbf{c}) = \frac{1}{2}\sum_{m=0}^{M-1}\|\underline{\mathbf{g}_m} - \mathbf{M}_m\mathbf{H}^c\mathbf{s}_m\|^2, \tag{9}$$

where $\underline{\mathbf{g}_m} \in \mathbb{R}^{N^{\mathrm{rec}}L}$ denotes the measured data vector at the m-th data acquisition. The choice of the penalty term will be addressed in Section IV.

The gradient of $\mathcal{F}(\mathbf{c})$ with respect to $\mathbf{c}$, denoted by $\mathbf{J}$, will be computed by discretizing an expression for the Fréchet derivative that is derived assuming a continuous form of Eqn. (9). The Fréchet derivative is described in Appendix B. Namely, the gradient is approximated as

$$[\mathbf{J}]_n \equiv \sum_{m=0}^{M-1}[\mathbf{J}_m]_n \approx \frac{1}{[\mathbf{c}]_n^3}\sum_{m=0}^{M-1}\sum_{l=1}^{L-2}[\mathbf{q}_m^{\mathrm{a}}]_{nL+(L-l)}\frac{[\mathbf{p}_m^{\mathrm{a}}]_{nL+l-1} - 2[\mathbf{p}_m^{\mathrm{a}}]_{nL+l} + [\mathbf{p}_m^{\mathrm{a}}]_{nL+l+1}}{\Delta^{\mathrm{t}}}, \tag{10}$$

where $\mathbf{J}_m$ denotes the gradient of $\frac{1}{2}\|\underline{\mathbf{g}_m} - \mathbf{M}_m\mathbf{H}^c\mathbf{s}_m\|^2$ with respect to $\mathbf{c}$ and the vector $\mathbf{q}_m^{\mathrm{a}}$ contains samples that approximate adjoint wavefield $q_m(\mathbf{r}, t)$ that satisfies Eqn. (33) in Appendix B. By use of the pseudospectral numerical solver, $\mathbf{q}_m^{\mathrm{a}}$ can be calculated by

$$\mathbf{q}_m^{\mathrm{a}} = \frac{1}{4\pi}\mathbf{H}^c\boldsymbol{\tau}_m, \tag{11}$$

where

$$[\boldsymbol{\tau}_m]_{nL+l} = \begin{cases} [\mathbf{g}_m^{\mathrm{a}} - \underline{\mathbf{g}}_m]_{\mathcal{I}_m^{-1}(n)L+(L-l)}, & \text{if } n \in \mathbb{N}_m, \\ 0, & \text{otherwise} \end{cases} . \tag{12}$$

Here, $\mathbb{N}_m = \{n : \mathcal{I}_m(n^{\mathrm{rec}}), n^{\mathrm{rec}} = 0, 1, \cdots, N^{\mathrm{rec}} - 1\}$, and $\mathcal{I}_m^{-1}$ denotes the inverse mapping of $\mathcal{I}_m$.

Given the explicit form of $\mathbf{J}$ in Eqn. (10), a variety of optimization algorithms can be employed to solve Eqn. (8) [39]. When a gradient descent algorithm is employed, the sequential waveform inversion method is given by Algorithm 1, where in Line-10, $\mathbf{J}^{\mathrm{R}}$ denotes the gradient of $\mathcal{R}(\mathbf{c})$ with respect to $\mathbf{c}$.

Algorithm 1 Gradient descent-based sequential waveform inversion.

Input: $\{\underline{\mathbf{g}}_m\}$, $\{\mathbf{s}_m\}$, $\mathbf{c}^{(0)}$

Output: $\hat{\mathbf{c}}$

  1: $k \leftarrow 0$ {k is the number of algorithm iteration.}

  2: **while** stopping criterion is not satisfied **do**

  3:        $k \leftarrow k + 1$

  4:        $\mathbf{J} \leftarrow \mathbf{0}$

  5:        **for** $m := 0$ **to** $M - 1$ **do**

  6:             $\mathbf{p}_m^{\mathrm{a}} \leftarrow \mathbf{H}^{\mathrm{c}} \mathbf{s}_m$ {m is the index of the emitter.}

  7:             $\mathbf{q}_m^{\mathrm{a}} \leftarrow \mathbf{H}^{\mathrm{c}} \boldsymbol{\tau}_m$ {$\boldsymbol{\tau}_m$ is calculated via Eqn. (12).}

  8:             $\mathbf{J} \leftarrow \mathbf{J} + \mathbf{J}_m$ {$\mathbf{J}_m$ is calculated via Eqn. (10).}

  9:        **end for**

10:        $\mathbf{J} \leftarrow \mathbf{J} + \beta \mathbf{J}^{\mathrm{R}}$

11:        Determine step size λ via a line search

12:        $\mathbf{c}^{(k)} \leftarrow \mathbf{c}^{(k-1)} - \lambda \mathbf{J}$

13: **end while**

14: $\hat{\mathbf{c}} = \mathbf{c}^{(k)}$

In Algorithm 1, $\mathbf{H}^{\mathrm{c}}$ is the most computationally burdensome operator, representing one run of the numerical solver. Note that it appears in Lines-6, -7, and -11. Because Lines-6 and -7 have to be executed M times to process all of the data acquisitions, the numerical solver has

to be executed at least $(2M + 1)$ times at each algorithm iteration. The line search in Line-11 searches for a step size along the direction of $-\mathbf{J}$ so that the cost function is reduced by use of a classic trial-and-error approach [39]. Note that, in general, the line search will require more than one application of $\mathbf{H}^c$, so $(2M + 1)$ represents a lower bound on the total number of numerical solver runs per iteration.

B. Stochastic optimization-based waveform inversion with source encoding (WISE)

In order to alleviate the large computational burden presented by sequential waveform inversion methods (e.g., Algorithm 1), a source encoding method has been proposed [22], [29], [40]. This method has been formulated as a stochastic optimization problem and solved by various stochastic gradient-based algorithms [30], [31]. In this section, we adapt the stochastic optimization-based formulation in [30] to find the solution of Eqn. (8).

The WISE method employs the same cost function given in Eqn. (8) except that the data fidelity term in Eqn. (9) is reformulated as the expectation of a random quantity as [29]–[31],

---

Algorithm 2 Waveform inversion with source encoding (WISE) algorithm.

Input: $\{\underline{\mathbf{g}}_m\}$, $\{\mathbf{s}_m\}$, $\mathbf{c}^{(0)}$

Output: $\hat{\mathbf{c}}$

  1: $k \leftarrow 0$ $\{k$ is the number of algorithm iteration$\}$

  2: **while** stopping criterion is not satisfied **do**

  3:       $k \leftarrow k + 1$

  4:       Draw elements of $\mathbf{w}$ from independent and identical Rademacher distribution.

  5:       $\mathbf{p}^{\mathrm{w}} \leftarrow \mathbf{H}^c \mathbf{s}^{\mathrm{w}}$ $\{\mathbf{s}^{\mathrm{w}}$ is calculated via Eqn. (14). $\}$

  6:       $\mathbf{q}^{\mathrm{w}} \leftarrow \mathbf{H}^c \boldsymbol{\tau}^{\mathrm{w}}$ $\{$See text for the calculation of $\boldsymbol{\tau}^{\mathrm{w}}\}$

  7:       $\mathbf{J} \leftarrow \mathbf{J}^{\mathrm{w}} + \beta \mathbf{J}^{\mathrm{R}}$ $\{\mathbf{J}^{\mathrm{w}}$ is calculated via Eqn. (16)$\}$

  8:       Determine step size λ by use of line search

  9:       $\mathbf{c}^{(k)} \leftarrow \mathbf{c}^{(k-1)} - \lambda \mathbf{J}^{\mathrm{w}}$

10: **end while**

11: $\hat{\mathbf{c}} = \mathbf{c}^{(k)}$

---

[33], [40], [41]

$$\mathcal{F}_s(\mathbf{c}) = \mathbf{E_w}\left\{\frac{1}{2}\|\underline{\mathbf{g}}^{\mathrm{w}} - \mathbf{MH}^{\mathrm{c}}\mathbf{s}^{\mathrm{w}}\|^2\right\}, \tag{13}$$

where $\mathbf{E_w}$ denotes the expectation operator with respect to the random source encoding vector $\mathbf{w} \in \mathbb{R}^M$, $\mathbf{M} \equiv \mathbf{M}_m$ is the sampling matrix that is assumed to be identical for $m = 0, 1, \cdots, M-1$, and $\underline{\mathbf{g}}^{\mathrm{w}}$ and $\mathbf{s}^{\mathrm{w}}$ denote the $\mathbf{w}$-encoded data and source vectors, defined as

$$\underline{\mathbf{g}}^{\mathrm{w}} = \sum_{m=0}^{M-1} [\mathbf{w}]_m \underline{\mathbf{g}}_m, \quad \text{and} \quad \mathbf{s}^{\mathrm{w}} = \sum_{m=0}^{M-1} [\mathbf{w}]_m \mathbf{s}_m, \tag{14}$$

respectively. It has been demonstrated that Eqns. (9) and (13) are mathematically equivalent when $\mathbf{w}$ possesses a zero mean and an identity covariance matrix [30], [33], [41]. In this case, the optimization problem whose solution specifies the sound speed estimate can be re-expressed in a stochastic framework as

$$\hat{\mathbf{c}} = \arg\min_{\mathbf{c}} \mathbf{E_w}\left\{\frac{1}{2}\|\underline{\mathbf{g}}^{\mathrm{w}} - \mathbf{MH}^{\mathrm{c}}\mathbf{s}^{\mathrm{w}}\|^2\right\} + \beta\mathcal{R}(\mathbf{c}), \tag{15}$$

which we refer to as the waveform inversion with source encoding (WISE) method. An implementation of the WISE method that utilizes the stochastic gradient descent algorithm is summarized in Algorithm 2.

In Algorithm 2, the numerical solver needs to be run one time in each of Lines 5 and 6. In the line search to determine the step size in Line 8, the numerical solver needs to be run at least one time, but in general will require a small number of additional runs, just as in Algorithm 1. Accordingly, the lower bound on the number of required numerical solver runs per iteration is 3, as opposed to $(2M+1)$ for the conventional sequential waveform inversion method described by Algorithm 1. As demonstrated in geophysics applications [29], [31], [40] and the breast imaging studies below, the WISE method provides a substantial reduction in reconstruction times over use of the standard sequential waveform inversion method. In Line-7, $\mathbf{J}^{\mathrm{w}}$ can be calculated analogously to Eqn. (10) as

$$[\mathbf{J}^{\mathrm{w}}]_n \approx \frac{1}{[\mathbf{c}]_n^3} \sum_{l=1}^{L-2} [\mathbf{q}^{\mathrm{w}}]_{nL+(L-l)} \frac{[\mathbf{p}^{\mathrm{w}}]_{nL+l-1} - 2[\mathbf{p}^{\mathrm{w}}]_{nL+l} + [\mathbf{p}^{\mathrm{w}}]_{nL+l+1}}{\Delta^{\mathrm{t}}}, \tag{16}$$

where $\mathbf{p}^{\mathrm{w}} = \mathbf{H}^{\mathrm{c}}\mathbf{s}^{\mathrm{w}}$ and $\mathbf{q}^{\mathrm{w}} = \mathbf{H}^{\mathrm{c}}\boldsymbol{\tau}^{\mathrm{w}}$. Various probablity density functions have been proposed to describe the random vector $\mathbf{w}$ [29], [31], [40]. In this study, we employed a Rademacher distribution as suggested by [29], in which case each element of $\mathbf{w}$ had a 50% chance of being either $+1$ or -1.

IV. Description of computer-simulation studies

Two-dimensional computer-simulation studies were conducted to validate the WISE method for breast sound speed imaging and demonstrate its computational advantage over the standard sequential waveform inversion method.

A. Measurement geometry

A circular measurement geometry was chosen to emulate a previously reported USCT breast imaging system [11], [23], [42]. As sketched in Fig. 1, 256 ultrasonic transducers were uniformly distributed on a ring of radius $R^s = 110$ mm. The generation of one USCT data set consisted of $M = 256$ sequential data acquisitions. In each data acquisition, one emitter produced an acoustic pulse. The acoustic pulse was numerically propagated through the breast phantom and the resulting wavefield data were recorded by all transducers in the array as described below. Note that the location of the emitter in every data acquisition was different from those in other acquisitions, while the locations of receivers were identical for all acquisitions.

B. Numerical breast phantom

A numerical breast phantom of diameter 98 mm was employed. The phantom was composed of 8 structures representing adipose tissues, parenchymal breast tissues, cysts, benign tumors, and malignant tumors, as shown in Fig. 2. For simplicity, the acoustic attenuation of all tissues was described by a power law with a fixed exponent $y = 1.5$ [43]. The corresponding sound speed values and the attenuation coefficients are listed in TABLE I [43]–[45]. Both the sound speed and the absorption coefficient distributions in Fig. 2 were sampled on a uniform Cartesian grid with spacing $\Delta^s = 0.25$ mm. The finest structure (indexed by 7 in Fig. 2-(a)) was of diameter 3.75 mm.

C. Simulation of the measurement data

1) First-order numerical wave equation solver: Acoustic wave propagation in acoustically absorbing media was modeled by three coupled first-order partial differential equations [46]:

$$\frac{\partial}{\partial t}\mathbf{u}(\mathbf{r},t) = -\nabla p(\mathbf{r},t) \tag{17a}$$

$$\frac{\partial}{\partial t}\rho(\mathbf{r},t) = -\nabla \cdot \mathbf{u}(\mathbf{r},t) + 4\pi \int_0^t dt' s(\mathbf{r},t') \tag{17b}$$

$$p(\mathbf{r},t) = c^2(\mathbf{r})\Big[1 + \tau(\mathbf{r})\frac{\partial}{\partial t}(-\nabla^2)^{y/2-1} + \eta(\mathbf{r})(-\nabla^2)^{(y+1)/2-1}\Big]\rho(\mathbf{r},t), \tag{17c}$$

where $\mathbf{u}(\mathbf{r},t)$, $p(\mathbf{r},t)$, and $\rho(\mathbf{r})$ denote the acoustic particle velocity, the acoustic pressure, and the acoustic density, respectively. The functions $\tau(\mathbf{r})$ and $\eta(\mathbf{r})$ describe acoustic absorption and dispersion during the wave propagation respectively [46]:

$$\tau(\mathbf{r}) = -2\alpha_0(\mathbf{r})c_0(\mathbf{r})^{y-1}, \quad \eta(\mathbf{r}) = 2\alpha_0(\mathbf{r})c_0(\mathbf{r})^y \tan(\pi y/2), \tag{18}$$

where $\alpha_0(\mathbf{r})$ and y are the absorption coefficient and the power law exponent respectively. When the medium is assumed to be lossless, i.e., $\alpha_0(\mathbf{r}) = 0$, it can be shown that Eqn. (17) is equivalent to Eqn. (1).

Based on Eqn. (17), a pseudospectral k-space method was employed to simulate acoustic pressure data [36], [46]. The numerical scheme will be referred to as a first-order numerical solver. The first-order numerical solver was implemented using graphic processing units (GPUs). The calculation domain was of size 512×512 mm^2, sampled on a 2048×2048 uniform Cartesian grid of spacing $\Delta^s = 0.25$ mm. A nearest-neighbor interpolation was employed to place all transducers on the grid points. On a platform consisting of dual quad-core CPUs with a 3.30 GHz clock speed, 64 gigabytes (GB) of random-accessing memory (RAM), and a single NVIDIA Tesla K20 GPU, the first-order numerical solver took 108 seconds to complete one foward simulation.

2) Acoustic excitation pulse: The excitation pulse employed in this study was assumed to be spatially localized at the emitter location while temporally it was a $f_c = 0.8$ MHz sinusoidal function tapered by a Gaussian kernel with standard deviation $\sigma = 0.5$ μs, i.e.,

$$s_m(\mathbf{r},t) = \begin{cases} \exp\big(-\frac{(t-t_c)^2}{2\sigma^2}\big)\sin(2\pi f_c t), & \text{at the } m\text{-th emitter location} \\ 0, & \text{otherwise}. \end{cases} \tag{19}$$

The temporal profile and the amplitude frequency spectrum of the excitation pulse are plotted in Fig. 3-(a) and -(b), respectively. The excitation pulse contained approximate 3 cycles.

3) Generation of non-attenuated and attenuated noise-free data: For every data acquisition, indexed by m, the first-order numerical wave equation solver was run for 3600 time steps with a time interval $\Delta^{\mathrm{t}} = 0.05\mu s$ (corresponding to a 20 MHz sampling rate). Downsampling the recorded data by taking every other time sample resulted in a data vector, i.e., $\underline{\mathbf{g}}_m$ in Eqn. (9), that was effectively sampled at 10 MHz and was of dimensions ML with $M = 256$ and $L = 1800$. The data vector at the 0-th data acquisition, $\underline{\mathbf{g}}_0$, is displayed as a 2D image in Fig. 4-(a). This undersampling procedure was introduced to avoid *inverse crime* [47] so that the data generation and the image reconstruction employed different numerical discretization schemes. Repeating the calculation for $m = 0, 1, \cdots, 255$, we obtained a collection $\{\underline{\mathbf{g}}_m\}$ of data vectors that together represented one complete data set. Utilizing the absorption phantom described in Section IV-B, a complete attenuated data set was computed. An idealized, non-attenuated, data set was also computed by setting $\alpha_0(\mathbf{r}) = 0$.

4) Generation of incomplete data: An incomplete data set in this study corresponds to one in which only N^{rec} receivers located on the opposite side of the emitter record the pressure wavefield, with $N^{\mathrm{rec}} < M$. Taking the 0-th data acquisition as an example (see Fig. 1), only $N^{\mathrm{rec}} = 100$ receivers, indexed from 78 to 177, record the wavefield, while other receivers record either unreliable or no measurements. Incomplete data sets formed in this way can emulate two practical scenarios: (1) Signals recored by receivers near the emitter are unreliable and therefore discarded [23]; and (2) An arc-shaped transducer array is employed that rotates with the emitter [14], [15], [48].

Specifically, incomplete data sets were generated as

$$\left[\underline{\mathbf{g}}_m^{\mathrm{incpl}}\right]_{n^{\mathrm{rec}}L+l} = \left[\underline{\mathbf{g}}_m\right]_{\mathcal{J}_m(n^{\mathrm{rec}})L+l}, \quad \text{for} \quad \substack{m=0,1,\cdots,M-1,\\ n^{\mathrm{rec}}=0,1,\cdots,N^{\mathrm{rec}}-1,} \tag{20}$$

where $\underline{\mathbf{g}}_m^{\mathrm{incpl}}$ is the incomplete m-th data acquisition, which is of dimensions $N^{\mathrm{rec}}L$, with $N^{\mathrm{rec}} < M$. The index map $\mathcal{J}_m : \{0, 1, \cdots, N^{\mathrm{rec}} - 1\} \mapsto \mathbb{M}_m^{\mathrm{good}}$ is defined as

$$\mathcal{J}_m(n^{\mathrm{rec}}) = \left(m + n^{\mathrm{rec}} + \frac{M - N^{\mathrm{rec}}}{2}\right) \mod M, \tag{21}$$

where $(m' \mod M)$ calculates the remainder of m' divided by M, and the index set $\mathbb{M}_m^{\mathrm{good}}$ collects indices of transducers that reliably record data at the m-th data acquisition and is defined as

$$\mathbb{M}_m^{\mathrm{good}} = \left\{k \mod M \,|\, k \in \left[m + (M - N^{\mathrm{rec}})/2, m + (M + N^{\mathrm{rec}})/2\right)\right\}. \tag{22}$$

Here, for simplicity, we assume both M and N^{rec} to be even numbers. In this study, we empirically set $N^{\text{rec}} = 100$ so that the object can be fully covered by the fan region as shown in Fig. 1.

5) Generation of noisy data: An additive Gaussian white noise model was employed to simulate electronic measurement noise as

$$\tilde{\mathbf{g}}_m = \underline{\mathbf{g}}_m + \tilde{\mathbf{n}}, \tag{23}$$

where $\tilde{\underline{\mathbf{g}}}_m$ and $\tilde{\mathbf{n}}$ are the noisy data vector and the Gaussian white noise vector, respectively. In this study, the maximum value of the pressure received by the 128-th transducer at the 0-th data acquisition with a homogeneous medium (water tank) was chosen as a reference signal amplitude. The noise standard deviation was set to be 5% of this value. An example of a simulated noiseless and noisy data acquisition is shown Fig. 4.

D. Image reconstruction

1) Second-order numerical wave equation solver: In the reconstruction methods described below, the action of the operator $\mathbf{H}^c$ (Eqn. (5)) was computed by solving Eqn. (1) by use of the pseudospectral k-space numerical solver method. This was implemented using GPUs. The calculation domain was of size 512×512 mm^2, sampled on a 1024×1024 uniform Cartesian grid of spacing $\Delta^{\text{s}} = 0.5$ mm for reconstruction. On a platform consisting of dual octa-core CPUs with a 2.00 GHz clock speed, 125 GB RAM, and a single NVIDIA Tesla K20C GPU, the second-order numerical solver, took 7 seconds to complete one forward simulation.

2) Sequential waveform inversion: To serve as a reference for the WISE method, we implemented the sequential waveform inversion method described in Algorithm 1. No penalty term was included ($\beta = 0$) because, due to its extreme computational burden, we only investigated this method in preliminary studies involving noise-free non-attenuated data. A uniform sound speed distribution was employed as the initial guess. We assumed that the background sound speed was known and the object was contained in a square region-of-interest (ROI) of dimension 128×128 mm^2 (See Fig. 1), which corresponded to 256×256 pixels.

3) WISE method: We implemented the WISE method according to Algorithm 2. Two types of smoothness penalties were employed in this study: a quadratic penalty expressed as

$$\mathcal{R}^{\text{Q}}(\mathbf{c}) = \sum_j \sum_i ([\mathbf{c}]_{jN_x+i} - [\mathbf{c}]_{jN_x+i-1})^2 + ([\mathbf{c}]_{jN_x+i} - [\mathbf{c}]_{(j-1)N_x+i})^2, \tag{24}$$

where N_x and N_y denote the number of grid points along the 'x' and 'y' directions respectively, and a total variation (TV) penalty, defined as [49], [50]

$$\mathcal{R}^{\mathrm{TV}}(\mathbf{c}) = \sum_j \sum_i \sqrt{\epsilon + ([\mathbf{c}]_{jN_x+i} - [\mathbf{c}]_{jN_x+i-1})^2 + ([\mathbf{c}]_{jN_x+i} - [\mathbf{c}]_{(j-1)N_x+i})^2}, \qquad (25)$$

where ϵ is a small number introduced to avoid dividing by 0 in the gradient calculation. In this study, we empirically selected $\epsilon = 10^{-8}$. The value was fixed because we observed that the value of ϵ had a minor impact on the reconstructed images compared to the impact of β. In addition, the use of this parameter can be avoided when advanced optimization algorithms are employed [51]. As in the sequential waveform inversion case, it was assumed that the background sound speed was known and the object was contained in a square ROI of dimension 128×128 mm^2 (See Fig. 1), which corresponded to 256×256 pixels. The regularization parameters corresponding to the quadratic penalty and the TV penalty will be denoted by β^{Q} and β^{TV}, respectively. Optimal regularization parameter values depend on the specific medically relavent task that the reconstructed images are used for [37]. Estimation of the optimal values requires a systematic investigation of the image statistics, which is out of the scope of this study. Here, we only investigated the impacts of β^{Q} and β^{TV} on the reconstructed images by sweeping their values over a wide range.

4) Reconstruction from incomplete data: Because the WISE method requires $\mathbf{M}_m$ to be identical for all m's, image reconstruction from incomplete data remains challenging [30], [33], [41]. In this study, two data completion strategies were investigated [30], [33], [41] to synthesize a complete data set, from which the WISE method could be effectively applied.

One strategy was to fill the missing data with pressure corresponding to a homogeneous medium as

$$[\underline{\mathbf{g}_m^{\mathrm{combH}}}]_{m^{\mathrm{rec}}L+l} = \begin{cases} [\underline{\mathbf{g}_m^{\mathrm{incpl}}}]_{\mathcal{J}_m^{-1}(m^{\mathrm{rec}})L+l}, & \text{if } m^{\mathrm{rec}} \in \mathbb{M}_m^{\mathrm{good}} \\ [\mathbf{g}_m^{\mathrm{h}}]_{m^{\mathrm{rec}}L+l}, & \text{otherwise}, \end{cases} \qquad (26)$$

for $m^{\mathrm{rec}} = 0, 1, \cdots, M-1$, where $\mathbf{g}_m^{\mathrm{h}} \in \mathbb{R}^{ML}$, $\underline{\mathbf{g}_m^{\mathrm{incpl}}} \in \mathbb{R}^{N^{\mathrm{rec}}L}$, and $\underline{\mathbf{g}_m^{\mathrm{combH}}} \in \mathbb{R}^{ML}$, denote the computer-simulated (with a homogeneous medium), the measured incomplete, and the combined complete data vectors at the m-th data acquisition, respectively. The mapping $\mathcal{J}_m^{-1} : \mathbb{M}_m^{\mathrm{good}} \mapsto \{0, 1, \cdots, N^{\mathrm{rec}} - 1\}$ denotes the inverse operator of $\mathcal{J}_m$ as

$$\mathcal{J}_m^{-1}(m^{\mathrm{rec}}) = \begin{cases} m^{\mathrm{rec}} - m - \frac{M-N^{\mathrm{rec}}}{2}, & \text{if } \frac{M-N^{\mathrm{rec}}}{2} \leq m^{\mathrm{rec}} - m < \frac{M+N^{\mathrm{rec}}}{2} \\ m^{\mathrm{rec}} - m + \frac{M+N^{\mathrm{rec}}}{2}, & \text{if } \frac{-M-N^{\mathrm{rec}}}{2} \leq m^{\mathrm{rec}} - m < \frac{-M+N^{\mathrm{rec}}}{2}. \end{cases} \qquad (27)$$

This data completion strategy is based on the assumption that the back-scatter from breast tissue in an appropriately sound speed-matched water bath is weak. This assumption suggests that the missing measurements can be replaced by the corresponding pressure data that would have been produced in the absence of the object.

The second, more crude, data completion strategy was to simply fill the missing data with zeros, i.e.,

$$[\underline{\mathbf{g}_m^{\text{comb0}}}]_{m^{\text{rec}}L+l} = \begin{cases} [\underline{\mathbf{g}_m^{\text{incpl}}}]_{\mathcal{J}_m^{-1}(m^{\text{rec}})L+l}, & \text{if} \quad m^{\text{rec}} \in \mathbb{M}_m^{\text{good}} \\ 0, & \text{otherwise}, \end{cases} \tag{28}$$

where $\underline{\mathbf{g}_m^{\text{comb0}}}$ denotes the data completed with the second strategy.

5) Bent-ray image reconstruction: A bent-ray method was also employed to reconstruct images. Details regarding the time-of-flight estimation and algorithm implemenations are provided in Appendix C.

V. COMPUTER-SIMULATION RESULTS

A. Images reconstructed from idealized data

The images reconstructed from the noise-free, non-attenuated, data by use of the WISE method with 199 iterations and the sequential waveform inversion method with 43 iterations are shown in Fig. 5-(a) and (b). As expected [23], [52], both images are more accurate and possess higher spatial resolution than the one reconstructed by use of the bent-ray reconstruction algorithm displayed in Fig. 5-(c). Profiles through the reconstructed images are displayed in Fig. 6. The images shown in Fig. 5-(a) and -(b) possess similar accuracies as measured by their Euclidean distances from the sound speed phantom vector $\mathbf{c}$; namely 0.07% of $\|\mathbf{c}\|$ for the former and 0.08% of $\|\mathbf{c}\|$ for the latter. However, the reconstruction of Fig. 5-(a) required only about 1.7% of the computational time required to reconstruct Fig. 5-(b); namely, 1.4 hours for the former and 81.4 hours for the latter respectively. This is because the WISE method required only 1018 numerical solver runs which is signficantly less than the 57088 numerical solver runs required by the sequential waveform inversion method. With a similar number of numerical solver runs, (e.g., 1024), one can only complete a single algorithm iteration by use of the sequential waveform inversion method. The corresponding image, shown in Fig. 5-(d), lacks quantitative accuracy as well as qualitative value for identifying features. The results suggest

that the WISE method maintains the advantages of the sequential waveform inversion method while significantly reducing the computational time.

B. Convergence of the WISE method

Images reconstructed from noise-free, non-attenuated, data by use of the WISE method contain radial streak artifacts when the algorithm iteration number is less than 100, as shown in Figs. 7-(a-c). Profiles through these images are displayed in 8. The streaks artifacts are likely caused by crosstalk introduced during the source encoding procedure [31], [40]. However, these artifacts are effectively mitigated after more iterations as demonstrated by the image reconstructed after the 199-th iteration in Fig. 5-(a) and its profile in Fig. 6. The quantitative accuracy of the reconstructed images is improved with more iterations as shown in Fig. 8.

Figure 9-(a) reveals that the WISE method requires a larger number of algorithm iterations than does the sequential waveform inversion method to achieve the same reconstruction accuracy, quantified by the Euclidean distance of the reconstructed image in percentage of $\|\mathbf{c}\|$. Also, the Euclidean distance of the reconstructed images by use of the WISE method appears to oscillate around 0.08% of $\|\mathbf{c}\|$ after the first 100 iterations while the sequential waveform inversion method can achieve a higher accuracy. However, as shown in Fig. 5-(a), the image reconstructed by use of the WISE method is highly accurate after the 199-th iteration. Moreover, to achieve the same accuracy, the amount of computation for the WISE method is about two-order of magnitude smaller than that for the sequential waveform inversion method as suggested by Fig. 9-(b). This is because of the significant computation reduction per iteration when the WISE method is employed. We also plotted the cost function value against the number of iterations in Fig. 9-(c). Note that for the WISE method, the cost function value was approximated by the current realization of $\frac{1}{2}\|\underline{\mathbf{g}}^{\mathrm{w}} - \mathbf{MH}^{\mathrm{c}}\mathbf{s}^{\mathrm{w}}\|^2$. These plots suggest that, in this particular case, the WISE method appears to approximately converge after 200 iterations. For example, the images reconstructed after 199 (Fig. 5-(a)) and 250 (Fig. 7-(d)) iterations are nearly identical.

C. Images reconstructed from non-attenuated data containing noise

Images reconstructed by use of the WISE method with a quadratic penalty and the WISE method with a TV penalty from noisy, non-attenutated, data are presented in Fig. 10. All images were obtained after 1024 algorithm iterations. The WISE method with a quadratic penalty

effectively mitigates image noise as shown in Figs. 10-(a-c), at the expense of image resolution, as expected. Figure 10-(d) shows an image reconstructed by use of the WISE method with a TV penalty. The image appears to possess a similar resolution but a lower noise level than the image in Fig. 10-(b) that was reconstructed by use of the WISE method with a quadratic penalty.

D. Images reconstructed from acoustically attenuated data

Our current implementation of the WISE method assumes an absorption-free acoustic medium. This assumption can be strongly violated in practice. In order to investigate the robustness of the the WISE method to model errors associated with ignoring medium acoustic absorption, we applied the algorithm to the acoustically attenuated data that were produced as described in Section IV-C. As shown in Fig. 11, when the medium acoustic absorption is considered, the amplitude of the measured pressure is attenuated by approximately a factor of 2. The wavefront (See Fig. 11-(a)) remains very similar to that when medium absorption is ignored (See Fig. 4-(a)). Medium absorption has the largest impact on the pressure data received by transducers located opposite the emitter as shown in Fig. 11-(b). The shape of the pulse profile remains very similar as shown in Fig. 11-(c) and -(d), suggesting that waveform dispersion may be less critical than amplitude attenuation in image reconstruction for this phantom.

Images reconstructed by use of the WISE method with a TV penalty from noise-free and noisy attenuated data are shown in Figs. 12-(a) and (b). Image profiles are shown in Fig. 12-(c). Although these images contain certain artifacts that were not produced in the idealized data studies, most object structures remain readily identified. These results suggest that the WISE method with a TV penalty can tolerate data inconsistencies associated with neglecting acoustic attenuation in the imaging model, at least to a certain level with regards to feature detection tasks.

E. Images reconstructed from idealized incomplete data

The wavefront of the noise- and attenuation-free pressure wavefield when the object is absent (Fig. 13-(a)) appears to be very similar to that when the object is present (Fig. 4-(a)). As expected, the largest differences are seen in the signals received by the transducers located opposite of the emitter, as shown in Fig. 13-(b). As seen in Fig. 13-(c), the time traces received

by the 40-th transducer are nearly identical when object is present and absent. This is because the back-scattered wavefield is weak for breast imaging applications. These results suggest the potential efficacy of the data completion strategy of filling the missing data with the pressure data corresponding to a water bath.

The image reconstructed from the measurements completed with pressure data corresponding to a water bath is shown in Fig.14-(a). As revealed by the profile in Fig.14-(c), this image is highly accurate. Alternatively, the image reconstructed from the the data completed with zeros contains strong artifacts as shown in Fig. 14-(b). These results suggest that the WISE method can be adapted to reconstruct images from incomplete data, which is particularly useful for emerging laser-induced USCT imaging systems [14]–[16].

VI. EXPERIMENTAL VALIDATION

A. Data acquisition

The SoftVue scanner was employed in the experimental study [53]. The scanner contained a ring-shaped transducer array of radius 110 mm. 2048 detecting elements were uniformly distributed on the ring. Each element had a center frequency of 2.75 MHz and a pitch of 0.34 mm. Each element was elevationally focused to isolate a slice of 3 mm in thickness. The transducer array was mounted in a water tank and could be translated with a motorized gantry in the vertical direction. We refer the readers to [53] for more details about the USCT imaging system.

The breast phantom was built by Dr. Ernie Madsen from the University of Wiscosin and provides tissue-equivalent scanning characteristics of highly scattering, predominantly parenchymal breast tissue. The phantom mimics the presence of benign and cancerous masses embedded in glandular tissue, including a subcutaneous fat layer. Figure 15 is a schematic plot of one phantom slice. The diameter of the inclusions is approximately 12 mm. Table II presents the known acoustic properties of the phantom.

During data acquisition, the breast phantom was placed near the center of the ring-shaped transducer array so that the distance between the phantom and each transducer was approximately the same. While scanning each slice, every other transducer element sequentially emits fan beam ultrasound signals towards the opposite side of the ring. The forward scattered and backscattered ultrasound signals are subsequently recorded by the same transducer elements. The received

waveform was sampled at a rate of 12 MHz. The 1024 data acquisitions took about 20 seconds in total. A calibration data set was also acquired with water bath only.

B. Data pre-processing

48 bad channels were manually identified by visual inspection. After discarding these, the data set contained $M = 976$ acquisitions. Each acquisition contained $N^{\text{rec}} = 976$ time traces. Each time trace contained $L = 2112$ time samples. The 976 good channels were indexed from 0 to 975. The corresponding data acquisitions were indexed in the same way. A Hann-window low-pass filter with a cutoff frequency of 4 MHz was applied to every time trace in both the calibration and the measurement data. This data filtering was implemented to mitigate numerical errors that could be introduced by our second-order numerical solver.

C. Estimation of excitation pulse

The shape of the excitation pulse was estimated as the time trace of the calibration data (after pre-processing) received by the 488-th receiver at the 0-th data acquisition. Note that the 488-th receiver was approximated located on the axis of the 0-th emitter, thus the received pulse was minimally affected by the finite aperture size effect of the transducers. Because our calibration data and measurement data were acquired using different electronic amplifier gains, the amplitude of the excitation pulse was estimated from the measurement data. More specifically, we simulated the 0-th data acquisition using our second-order numerical solver and compared the simulated time trace received by the 300-th receiver with the corresponding measured time trace (after pre-processing). The ratio between the maximum values of these two traces was used to scale the excitation pulse shape. We selected the 300-th receiver because it resided out of the fan-region indicated in Fig. 1; its received signals were unlikely to be strongly affected by the presence of the object. The estimated excitation pulse and its amplitude spectrum are displayed in Fig. 16. Note that the experimental excitation pulse contained higher frequency components than did the computer-simulated excitation pulse shown in Fig. 3.

D. Synthesis of combined data

As discussed in Section IV-C4, signals received by receivers located near the emitter can be unreliable [23]. Our experimental data, as shown in Fig. 17-(a), contained noise-like measurements for the receivers indexed from 0 to 200, and from 955 to 975, in the case where the 0-th

transducer functioned as the emitter. Also, our point-like transducer assumption introduces larger model mismatches for the receivers located near the emitter. As shown in Figs. 17-(c) and -(d), even though the simulated time trace received by the 300-th receiver matches accurately with the experimentally measured one, the simulated time trace received by the 200-th receiver is substantially different compared with the experimentally measured one. In order to minimize the effects of model mismatch, we replaced these unreliable measurements with computer-simulated water bath data, as described in Section IV-C. We designated the time traces received by the 512 receivers located on the opposite side of the emitter as the reliable measurements for each data acquisition. The 0-th data acquisition of the combined data is displayed in Fig. 17-(b).

E. Estimation of initial guess

The initial guess for the WISE method was obtained by use of the bent-ray reconstruction method described in Appendix C. We first filtered each time trace of the raw data by a band-pass butterworth filter (0.5MHz - 2.5MHz). Subsequently, we extracted the TOF by use of the thresholding method with a thresholding value of 20% of the peak value of each time trace. The bent-ray reconstruction algorithm was applied for image reconstruction with a measured background sound speed 1.513 mm/μs. The resulting image is shown in Fig. 18-(a) and has a pixel size of 1 mm. Finally, the image was smoothed by convolving it with a 2D Gaussian kernel with a standard deviation of 2 mm.

F. Image reconstruction

We applied the WISE method with a TV penalty to the combined data set. The second-order numerical solver was employed with a calculation domain of dimensions 512.0×512.0 mm^2. The calculation domain was sampled on a 2560×2560 Cartesian grid with a grid spacing of 0.2 mm. On a platform consisting of dual quad-core CPUs with a 3.30 GHz clock speed, 64 GB RAM, and a single NVIDIA Tesla K20 GPU, each numerical solver run, took 40 seconds to calculate the pressure data for 2112 time samples. Knowing the size of the phantom, we set the reconstruction region to be within a circle of diameter 128 mm, i.e., only the sound speed values of pixels within the circle were updated during the iterative image reconstruction. We swept the value of β^{TV} over a wide range to investigate its impact on the reconstructed images.

G. Images reconstructed from experimental data

As shown in Fig. 18, the spatial resolution of the image reconstructed by use of the WISE method with a TV penalty is significantly higher than that reconstructed by use of the bent-ray model-based method. In particular, the structures labeled 'A' and 'B' possess clearly-defined boundaries. This observation is further confirmed by the profiles of the two images shown in Fig. 19. In addition, the structure labeled 'C' in Fig. 18-(b) is almost indistinguishable in the image reconstructed by use of the bent-ray model-based method (see Fig. 18-(a)). The improved spatial resolution is expected because the WISE method with a TV penalty takes into account the high-order diffraction, which is ignored by the bent-ray method [23]. Though not shown here, for the bent-ray method, we investigated multiple time-of-flight pickers [25], and systematically tuned the regularization parameter. As such, it is likely that Fig. 18-(a) represents a nearly optimal bent-ray image in terms of the resolution. This resolution also appears to be similar to previous experimental results reported in the literature [26].

The convergence properties of the WISE method with a TV penalty with experimental data were consistent with those observed in the computer-simulation studies. Images reconstructed by use of 10, 50, and 300 algorithm iterations are displayed in Fig. 20. The image reconstructed by use of 10 iterations contains radial streak artifacts that are similar in nature to those observed in the computer-simulation studies. These artifacts were mitigated after more iterations. The image reconstructed after 300 iterations (Fig. 20-(d)) appears to be similar to that after 200 iterations (Fig. 18-(b)), suggesting that the WISE method with a TV penalty is close to convergence after about 200 iterations. The computational time for completing 200 iterations was approximately 14 hours. The estimated computational time for the conventional method was about one month, assuming the same number of iterations is required as in the computer-simulation studies (i.e., 40).

Despite the nonlinearity of the WISE method with a TV penalty, the impact of the TV smoothness penalty appears to be similar to that observed in other imaging applications [51], [54] (see Fig. 21). Though not shown here, the impact of the quadratic penalty is also similar. As expected, a larger value of β reduced the noise level at the expense of spatial image resolution. These results suggest a predictable impact of the smoothness penalties on the images reconstructed using the WISE method with a TV penalty.

VII. Summary

It is known that waveform inversion-based reconstruction methods can produce sound speed images that possess improved spatial resolution properties over those produced by ray-based methods. However, waveform inversion methods are computationally demanding and have not been applied widely in USCT breast imaging. In this work, based on the time-domain wave equation and motivated by recent mathematical results in the geophysics literature, the WISE method was developed that circumvents the large computational burden of conventional waveform inversion methods. This method encodes the measurement data using a random encoding vector and determines an estimate of the sound speed distribution by solving a stochastic optimization problem by use of a stochastic gradient descent algorithm. With our current GPU-based implementation, the computation time was reduced from weeks to hours. The WISE method was systematically investigated in computer-simulation and experimental studies involving a breast phantom. The results suggest that the method holds value for USCT breast imaging applications in a practical setting.

Many opportunities remain to further improve the performance of the WISE method. As shown in Fig. 18, images reconstructed by use of the WISE method can contain certain artifacts that are not present in the image reconstructed by use of the bent-ray method. An example of such an artifact is the dark horizontal streak below the structure C. Because of the nonlinearilty of the image reconstruction problem, it is challenging to determine whether these artifacts are caused by imaging model errors or by the optimization algorithm, which might have arrived at a local minimum of the cost function. A more accurate imaging model can be developed to account for the out-of-plane scattering, the transducer finite aperture size effect, and the medium acoustic absorption, etc. Also, the stochastic gradient descent algorithm is one of the most basic stochastic optimization algorithms. Numerous emerging optimization algorithms can be employed [33], [41] to improve the convergence rate, as well as to avoid local minima.

There remains a need to conduct additional investigations of the numerical properties of the WISE method. Currently, a systematic comparsion of the statistical properties of the WISE and the sequential waveform inversion methods is prohibted by the 3-day computational time for the latter method. This comparsion will be interesting when a more efficient numerical solver is available. Given the fact that waveform inversion is nonlinear and sensitive to its initial guess,

it becomes important to investigate how to obtain an accurate and computationally efficient initial guess. We also observed that the performance of the WISE method is sensitive to how strong the medium heterogeneities are and the profile of the excitation pulse. Investigation of the impact of the excitation pulse on the image reconstruction may help optimize hardware design. In addition, exploring the statistics of the reconstructed images will allow a quantitative image quality assessment for cancer diagnosis.

APPENDIX A
CONTINUOUS-TO-DISCRETE USCT IMAGING MODEL

In practice, each data function $g_m(\mathbf{r}, t)$ is spatially and temporally sampled to form a data vector $\mathbf{g}_m \in \mathbb{R}^{N^{\text{rec}}L}$, where N^{rec} and L denote the number of receivers and the number of time samples, respectively. We will assume that N^{rec} and L do not vary with excitation pulse. Let $[\mathbf{g}_m]_{n^{\text{rec}}L+l}$ denotes the $(n^{\text{rec}}L + l)$-th element of $\mathbf{g}_m$. When the receivers are point-like, $\mathbf{g}_m$ is defined as

$$[\mathbf{g}_m]_{n^{\text{rec}}L+l} = g_m(\mathbf{r}(m, n^{\text{rec}}), l\Delta^{\text{t}}), \tag{29}$$

where the indices n^{rec} and l specify the receiver location and temporal sample, respectively, and Δ^{t} is the temporal sampling interval. The vector $\mathbf{r}(m, n^{\text{rec}}) \in \Omega_m$ denotes the location of the n^{rec}-th receiver at the m-th data acquisition.

A C-D imaging model for USCT describes the mapping of $c(\mathbf{r})$ to the data vector $\mathbf{g}_m$ and can be expressed as

$$[\mathbf{g}_m]_{n^{\text{rec}}L+l} = \mathcal{M}_m \mathcal{H}^{\text{c}} s_m(\mathbf{r}, t)\big|_{\mathbf{r}=\mathbf{r}(m,n^{\text{rec}}), t=l\Delta^{\text{t}}} \quad \text{for} \quad \begin{smallmatrix} n^{\text{rec}}=0,1,\cdots,N^{\text{rec}}-1 \\ l=0,1,\cdots,L-1 \end{smallmatrix}. \tag{30}$$

Note that the acousto-electrical impulse response of the receivers can be incorporated into the C-D imaging model by temporally convolving $s_m(\mathbf{r}, t)$ in Eqn. (1) with the receivers' acousto-electrical impulse response if we assume all receiving transducers share an identical acousto-electrical impulse response.

APPENDIX B
FRÉCHET DERIVATIVE OF DATA FIDELITY TERM

Consider the integrated squared-error data misfit function, [22], [23]

$$\mathcal{F}^{\text{CC}}(c) = \frac{1}{2} \sum_{m=0}^{M-1} \int_{\Omega_m} d\mathbf{r} \int_0^T dt \big[\underline{g_m}(\mathbf{r}, t) - g_m(\mathbf{r}, t)\big]^2, \tag{31}$$

where $\underline{g_m}(\mathbf{r}, t)$ and $g_m(\mathbf{r}, t)$ denote the measured data function and the predicted data function computed by use of Eqn. (3) with the current estimate of $c(\mathbf{r})$.

Both the sequential and WISE reconstruction method described in Section III require knowledge of the Fréchet derivatives of $\mathcal{F}^{\mathrm{CC}}(c)$ and $\mathcal{R}^{\mathrm{CC}}(c)$ with respect to c, denoted by $\nabla_c \mathcal{F}^{\mathrm{CC}}$ and $\nabla_c \mathcal{R}^{\mathrm{CC}}$, respectively. The calculation of $\nabla_c \mathcal{R}^{\mathrm{CC}}$ can be readily accomplished for quadratic smoothness penalties [51], [55]. For the integrated squared error data misfit function given in Eqn. (31), $\nabla_c \mathcal{F}^{\mathrm{CC}}$ can be computed via an adjoint state method as [28], [56], [57]

$$\nabla_c \mathcal{F}^{\mathrm{CC}} = \frac{1}{c^3(\mathbf{r})} \sum_{m=0}^{M-1} \int_0^T dt\, q_m(\mathbf{r}, T-t) \frac{\partial^2}{\partial^2 t} p_m(\mathbf{r}, t), \tag{32}$$

where $q_m(\mathbf{r}, t) \in \mathbb{L}^2(\mathbb{R}^3 \times [0, \infty))$ is the solution to the adjoint wave equation. The adjoint wave equation is defined as

$$\nabla^2 q_m(\mathbf{r}, t) - \frac{1}{c^2(\mathbf{r})} \frac{\partial^2}{\partial^2 t} q_m(\mathbf{r}, t) = -\tau_m(\mathbf{r}, t), \tag{33}$$

where $\tau_m(\mathbf{r}, t) = g_m(\mathbf{r}, T-t) - \underline{g_m}(\mathbf{r}, T-t)$. The adjoint wave equation is nearly identical in form to the wave equation in Eqn. (1) except for the different source term on the right-hand side, suggesting the same numerical approach can be employed to solve both equations. Since one needs to solve Eqns. (1) and (33) M times in order to calculate $\nabla_c \mathcal{F}^{\mathrm{CC}}$, it is generally true that the sequential waveform inversion is computationally demanding even for a 2D geometry [58].

APPENDIX C

BENT-RAY MODEL-BASED SOUND SPEED RECONSTRUCTION

We developed an iterative image reconstruction algorithm based on a bent-ray imaging model. The bent-ray imaging model assumes that an acoustic pulse travels along a ray path that connects the emitter and the receiver and accounts for the refraction of rays, also known as ray-bending, through an acoustically inhomogeneous medium. For each pair of receiver and emitter, the travel time, as well as the ray path, is determined by the medium's sound speed distribution. Given the travel times for a collection of emitter-and-receiver pairs distributed around the object, the medium sound speed distribution can be iteratively reconstructed. This bent-ray model-based sound speed reconstruction (BRSR) method has been employed in the USCT literature [26], [59], [60].

In order to perform the BRSR, we extracted a TOF data vector from the measured pressure data. Denoting the TOF data vector by $\underline{\mathbf{T}} \in \mathbb{R}^{MN^{\text{rec}}}$, each element of $\underline{\mathbf{T}}$ represented the TOF from each emitter-and-receiver pair. The extraction of the TOF was conducted in two steps. First, we estimated the difference between the TOF when the object was present and the TOF when the object was absent by use of a thresholding method [25], [61]. In particular, 20% of the peak value of each time trace was employed as the thresholding value. Second, a TOF offset was added to the estimated difference TOF for each emitter-and-receiver pair to obtain the absolute TOF, where the TOF offset was calculated according to the scanning geometry and the known background SOS.

Having the TOF vector $\underline{\mathbf{T}}$, we reconstructed the sound speed by solving the following optimization problem:

$$\hat{\mathbf{s}} = \arg\min_{\mathbf{s}} \parallel \underline{\mathbf{T}} - \mathbf{K}^{\text{s}}\mathbf{s} \parallel^2 + \beta\mathcal{R}(\mathbf{s}), \tag{34}$$

where $\mathbf{s}$ denotes the slowness (the reciprocal of the SOS) vector, and $\mathbf{K}^{\text{s}}$ denotes the system matrix that maps the slowness distribution to the TOF data. The superscript 's' indicates the dependence of $\mathbf{K}^{\text{s}}$ on the slowness map. At each iteration, using the current estimate of the SOS, a ray-tracing method [62] was employed to construct the system matrix $\mathbf{K}^{\text{s}}$. Explicitly storing the system matrix in the sparse representation, we utilized the limited BFGS method [63] to solve the optimization problem given in Eqn. (34). The estimated slowness was then converted to the sound speed by taking the reciprocal of $\hat{\mathbf{s}}$ element-wisely. We refer the readers to [26], [59]–[61], [64] for more details about the BRSR method.

REFERENCES

[1] G. Glover, "Characterization of in vivo breast tissue by ultrasonic time-of-flight computed tomography," in *Natl Bur Stand Int Symp Ultrason Tissue Characterization, National Science Foundation, Ultrasonic Tissue Characterization II*, 1979, pp. 221–225.

[2] P. Carson, C. Meyer, A. Scherzinger, and T. Oughton, "Breast imaging in coronal planes with simultaneous pulse echo and transmission ultrasound," *Science*, vol. 214, no. 4525, pp. 1141–1143, 1981. [Online]. Available: http://www.sciencemag.org/content/214/4525/1141.abstract

[3] J. S. Schreiman, J. J. Gisvold, J. F. Greenleaf, and R. C. Bahn, "Ultrasound transmission computed tomography of the breast." *Radiology*, vol. 150, no. 2, pp. 523–530, 1984, pMID: 6691113. [Online]. Available: http://pubs.rsna.org/doi/abs/10.1148/radiology.150.2.6691113

[4] M. P. André, H. S. Janée, P. J. Martin, G. P. Otto, B. A. Spivey, and D. A. Palmer, "High-speed data acquisition in a diffraction tomography system employing large-scale toroidal arrays," *International Journal of Imaging Systems and Technology*, vol. 8, no. 1, pp. 137–147, 1997.

[5] P. Carson, C. Meyer, A. Scherzinger, and T. Oughton, "Breast imaging in coronal planes with simultaneous pulse echo and transmission ultrasound," *Science*, vol. 214, no. 4525, pp. 1141–1143, 1981. [Online]. Available: http://www.sciencemag.org/content/214/4525/1141.abstract

[6] D. T. Borup, S. A. Johnson, F. Natterer, S. C. Olsen, J. W. Wiskin, F. Wubeling, and Y. Zhang, "Apparatus and method for imaging with wavefields using inverse scattering techniques," Dec. 21 1999, uS Patent 6,005,916.

[7] N. Duric, P. Littrup, L. Poulo, A. Babkin, R. Pevzner, E. Holsapple, O. Rama, and C. Glide, "Detection of breast cancer with ultrasound tomography: First results with the computed ultrasound risk evaluation (CURE) prototype," *Medical physics*, vol. 34, no. 2, pp. 773–785, 2007.

[8] N. V. Ruiter, G. Göbel, L. Berger, M. Zapf, and H. Gemmeke, "Realization of an optimized 3D USCT," in *SPIE Medical Imaging*. International Society for Optics and Photonics, 2011, pp. 796 805–796 805.

[9] N. Duric, O. Roy, C. Li, S. Schmidt, X. Cheng, J. Goll, D. Kunz, K. Bates, R. Janer, and P. Littrup, "Ultrasound tomography systems for medical imaging," in *Emerging Imaging Technologies in Medicine*. CRC Press, 2012, pp. 167–182.

[10] N. V. Ruiter, M. Zapf, T. Hopp, R. Dapp, E. Kretzek, M. Birk, B. Kohout, and H. Gemmeke, "3D ultrasound computer tomography of the breast: A new era?" *European Journal of Radiology*, vol. 81, Supplement 1, no. 0, pp. S133 – S134, 2012, extended abstracts and Abstracts of the Sixth International Congress on MR-Mammography. [Online]. Available: http://www.sciencedirect.com/science/article/pii/S0720048X12700554

[11] N. Duric, P. Littrup, O. Roy, S. Schmidt, C. Li, L. Bey-Knight, and X. Chen, "Breast imaging with ultrasound tomography: Initial results with softvue," in *Ultrasonics Symposium (IUS), 2013 IEEE International*, July 2013, pp. 382–385.

[12] C. Li, N. Duric, P. Littrup, and L. Huang, "In vivo breast sound-speed imaging with ultrasound tomography," *Ultrasound in Medicine & Biology*, vol. 35, no. 10, pp. 1615 – 1628, 2009. [Online]. Available: http://www.sciencedirect.com/science/article/pii/S03015629090002373

[13] J. Wiskin, D. T. Borup, S. A. Johnson, and M. Berggren, "Non-linear inverse scattering: High resolution quantitative breast tissue tomography," *J. Acoust. Soc. Am.*, vol. 131, no. 5, pp. 3802–3813, 2012. [Online]. Available: http://scitation.aip.org/content/asa/journal/jasa/131/5/10.1121/1.3699240

[14] S. Manohar, R. G. H. Willemink, F. van der Heijden, C. H. Slump, and T. G. van Leeuwen, "Concomitant speed-of-sound tomography in photoacoustic imaging," *Applied Physics Letters*, vol. 91, p. 131911, 2007.

[15] J. Zalev, D. Herzog, B. Clingman, T. Miller, K. Kist, N. C. Dornbluth, B. M. McCorvey, P. Otto, S. Ermilov, V. Nadvoretsky *et al.*, "Clinical feasibility study of combined optoacoustic and ultrasonic imaging modality providing coregistered functional and anatomical maps of breast tumors," in *SPIE BiOS*. International Society for Optics and Photonics, 2012, pp. 82 230A– 82 230A.

[16] J. Xia, C. Huang, K. Maslov, M. A. Anastasio, and L. V. Wang, "Enhancement of photoacoustic tomography by ultrasonic computed tomography based on optical excitation of elements of a full-ring transducer array," *Opt. Lett.*, vol. 38, no. 16, pp. 3140–3143, Aug 2013. [Online]. Available: http://ol.osa.org/abstract.cfm?URI=ol-38-16-3140

[17] A. C. Kak and M. Slaney, *Principles of Computerized Tomographic Imaging*. IEEE Press, 1988.

[18] R. J. Lavarello and M. L. Oelze, "Density imaging using inverse scattering," *J. Acoust. Soc. Am.*, vol. 125, no. 2, pp. 793–802, 2009. [Online]. Available: http://scitation.aip.org/content/asa/journal/jasa/125/2/10.1121/1.3050249

[19] ——, "Density imaging using a multiple-frequency DBIM approach," *IEEE. T. Ultrason. Ferr.*, vol. 57, no. 11, pp. 2471–2479, November 2010.

[20] A. J. Hesford and W. C. Chew, "Fast inverse scattering solutions using the distorted born iterative method and the multilevel fast multipole algorithm," *J. Acoust. Soc. Am.*, vol. 128, no. 2, 2010.

[21] P. Huthwaite and F. Simonetti, "High-resolution imaging without iteration: a fast and robust method for breast ultrasound tomography," *J. Acoust. Soc. Am.*, vol. 130, no. 3, pp. 1721–1734, 2011. [Online]. Available: http://scitation.aip.org/content/asa/journal/jasa/130/3/10.1121/1.3613936

[22] Z. Zhang, L. Huang, and Y. Lin, "Efficient implementation of ultrasound waveform tomography using source encoding," in *SPIE Medical Imaging*. International Society for Optics and Photonics, 2012, pp. 832 003–832 003.

[23] R. G. Pratt, L. Huang, N. Duric, and P. Littrup, "Sound-speed and attenuation imaging of breast tissue using waveform tomography of transmission ultrasound data," in *Proc. SPIE*, vol. 6510, 2007, pp. 65 104S–65 104S–12. [Online]. Available: http://dx.doi.org/10.1117/12.708789

[24] P. Huthwaite, F. Simonetti, and N. Duric, "Combining time of flight and diffraction tomography for high resolution breast imaging: Initial in vivo results (l)," *J. Acoust. Soc. Am.*, vol. 132, no. 3, pp. 1249–1252, 2012. [Online]. Available: http://scitation.aip.org/content/asa/journal/jasa/132/3/10.1121/1.4742697

[25] C. Li, L. Huang, N. Duric, H. Zhang, and C. Rowe, "An improved automatic time-of-flight picker for medical ultrasound tomography," *Ultrasonics*, vol. 49, no. 1, pp. 61–72, 2009.

[26] A. Hormati, I. Jovanovi, O. Roy, and M. Vetterli, "Robust ultrasound travel-time tomography using the bent ray model," in *Proc. SPIE*, vol. 7629, 2010, pp. 76 290I–76 290I–12. [Online]. Available: http://dx.doi.org/10.1117/12.844693

[27] R. Bates, V. Smith, and R. Murch, "Manageable multidimensional inverse scattering theory," *Phys. Rep.*, vol. 201, no. 4, pp. 185 – 277, 1991. [Online]. Available: http://www.sciencedirect.com/science/article/pii/037015739190026I

[28] O. Roy, I. Jovanović, A. Hormati, R. Parhizkar, and M. Vetterli, "Sound speed estimation using wave-based ultrasound tomography: theory and GPU implementation," in *SPIE Medical Imaging*. International Society for Optics and Photonics, 2010, pp. 76 290J–76 290J.

[29] J. R. Krebs, J. E. Anderson, D. Hinkley, R. Neelamani, S. Lee, A. Baumstein, and M.-D. Lacasse, "Fast full-wavefield seismic inversion using encoded sources," *Geophysics*, vol. 74, no. 6, pp. WCC177–WCC188, 2009.

[30] E. Haber, M. Chung, and F. Herrmann, "An effective method for parameter estimation with PDE constraints with multiple right-hand sides," *SIAM J. Optimiz.*, vol. 22, no. 3, pp. 739–757, 2012. [Online]. Available: http://epubs.siam.org/doi/abs/10.1137/11081126X

[31] P. P. Moghaddam, H. Keers, F. J. Herrmann, and W. A. Mulder, "A new optimization approach for source-encoding full-waveform inversion," *Geophysics*, vol. 78, no. 3, pp. R125–R132, 2013. [Online]. Available: http://geophysics.geoscienceworld.org/content/78/3/R125.abstract

[32] J. Wiskin, D. Borup, S. Johnson, M. Andre, J. Greenleaf, Y. Parisky, and J. Klock, "Three-dimensional nonlinear inverse scattering: Quantitative transmission algorithms, refraction corrected reflection, scanner design and clinical results," *Proceedings of Meetings on Acoustics*, vol. 19, no. 1, 2013. [Online]. Available: http://scitation.aip.org/content/asa/journal/poma/19/1/10.1121/1.4800267

[33] E. Haber and M. Chung, "Simultaneous source for non-uniform data variance and missing data," *arXiv preprint arXiv:1404.5254*, 2014.

[34] K. W. Morton and D. F. Mayers, *Numerical Solution of Partial Differential Equations: An Introduction*. New York, NY, USA: Cambridge University Press, 2005.

[35] T. Mast, L. Souriau, D.-L. Liu, M. Tabei, A. Nachman, and R. Waag, "A k-space method for large-scale models of wave propagation in tissue," *Ultrasonics, Ferroelectrics and Frequency Control, IEEE Transactions on*, vol. 48, no. 2, pp. 341–354, March 2001.

[36] M. Tabei, T. D. Mast, and R. C. Waag, "A k-space method for coupled first-order acoustic propagation equations," *J. Acoust. Soc. Am.*, vol. 111, no. 1, pp. 53–63, 2002. [Online]. Available: http://scitation.aip.org/content/asa/journal/jasa/111/1/10.1121/1.1421344

[37] H. Barrett and K. Myers, *Foundations of Image Science*. Wiley Series in Pure and Applied Optics, 2004.

[38] L. E. Kinsler, A. R. Frey, A. B. Coppens, and J. V. Sanders, *Fundamentals of acoustics*, 4th ed. Wiley, Dec. 2000. [Online]. Available: http://www.amazon.com/exec/obidos/redirect?tag=citeulike07-20&path=ASIN/0471847895

[39] S. Nash and A. Sofer, *Linear and Nonlinear Programming*. New York: McGraw-Hill, 1996.

[40] L. A. Romero, D. C. Ghiglia, C. C. Ober, and S. A. Morton, "Phase encoding of shot records in prestack migration," *Geophysics*, vol. 65, no. 2, pp. 426–436, 2000.

[41] F. Roosta-Khorasani, K. van den Doel, and U. M. Ascher, "Data completion and stochastic algorithms for PDE inversion problems with many measurements," *CoRR*, vol. abs/1312.0707, 2013.

[42] N. Duric, P. Littrup, S. Schmidt, C. Li, O. Roy, L. Bey-Knight, R. Janer, D. Kunz, X. Chen, J. Goll, A. Wallen, F. Zafar, V. Allada, E. West, I. Jovanovic, K. Li, and W. Greenway, "Breast imaging with the softvue imaging system: first results," in *Proc. SPIE*, vol. 8675, 2013, pp. 86 750K–86 750K–8. [Online]. Available: http://dx.doi.org/10.1117/12.2002513

[43] T. L. Szabo, *Diagnostic ultrasound imaging: inside out*. Academic Press, 2004.

[44] C. Glide, N. Duric, and P. Littrup, "Novel approach to evaluating breast density utilizing ultrasound tomography," *Medical Physics*, vol. 34, no. 2, pp. 744–753, 2007. [Online]. Available: http://scitation.aip.org/content/aapm/journal/medphys/34/2/10.1118/1.2428408

[45] C. Li, N. Duric, and L. Huang, "Clinical breast imaging using sound-speed reconstructions of ultrasound tomography data," in *Proc. SPIE*, vol. 6920, 2008, pp. 692 009–692 009–9. [Online]. Available: http://dx.doi.org/10.1117/12.771436

[46] B. E. Treeby, E. Z. Zhang, and B. T. Cox, "Photoacoustic tomography in absorbing acoustic media using time reversal," *Inverse Problems*, vol. 26, no. 11, p. 115003, 2010. [Online]. Available: http://stacks.iop.org/0266-5611/26/i=11/a=115003

[47] D. Colton and R. Kress, *Inverse acoustic and electromagnetic scattering theory*. Springer, 2012, vol. 93.

[48] S. A. Ermilov, R. Su, A. Conjusteau, V. Ivanov, V. Nadvoretskiy, T. Oruganti, P. Talole, F. Anis, M. A. Anastasio, and A. A. Oraevsky, "3D laser optoacoustic ultrasonic imaging system for research in mice (LOUIS-3DM)," in *Proc. SPIE*, vol. 8943, 2014, pp. 89 430J–89 430J–6. [Online]. Available: http://dx.doi.org/10.1117/12.2044817

[49] E. Y. Sidky and X. Pan, "Image reconstruction in circular cone-beam computed tomography by constrained, total-variation minimization," *Phys. Med. Biol.*, vol. 53, no. 17, p. 4777, 2008, http://stacks.iop.org/0031-9155/53/i=17/a=021.

[50] K. Wang, E. Y. Sidky, M. A. Anastasio, A. A. Oraevsky, and X. Pan, "Limited data image reconstruction in optoacoustic tomography by constrained total variation minimization," A. A. Oraevsky and L. V. Wang, Eds., vol. 7899, no. 1. SPIE, 2011, p. 78993U. [Online]. Available: http://link.aip.org/link/?PSI/7899/78993U/1

[51] K. Wang, R. Su, A. A. Oraevsky, and M. A. Anastasio, "Investigation of iterative image reconstruction in three-dimensional optoacoustic tomography," *Phys. Med. Biol.*, vol. 57, no. 17, p. 5399, 2012. [Online]. Available: http://stacks.iop.org/0031-9155/57/i=17/a=5399

[52] C. Li, G. S. Sandhu, O. Roy, N. Duric, V. Allada, and S. Schmidt, "Toward a practical ultrasound waveform tomography

algorithm for improving breast imaging," in *Proc. SPIE*, vol. 9040, 2014, pp. 90 401P–90 401P–10. [Online]. Available: http://dx.doi.org/10.1117/12.2043686

[53] N. Duric, P. Littrup, C. Li, O. Roy, S. Schmidt, X. Cheng, J. Seamans, A. Wallen, and L. Bey-Knight, "Breast imaging with softvue: initial clinical evaluation," vol. 9040, 2014, pp. 90 400V–90 400V–8. [Online]. Available: http://dx.doi.org/10.1117/12.2043768

[54] K. Wang, R. Schoonover, R. Su, A. Oraevsky, and M. A. Anastasio, "Discrete imaging models for three-dimensional optoacoustic tomography using radially symmetric expansion functions," *Medical Imaging, IEEE Transactions on*, vol. 33, no. 5, pp. 1180–1193, May 2014.

[55] J. A. Fessler, "Penalized weighted least-squares reconstruction for positron emission tomography," *IEEE T. Med. Imaging*, vol. 13, pp. 290–300, 1994.

[56] S. J. Norton, "Iterative inverse scattering algorithms: Methods of computing Fréchet derivatives," *J. Acoust. Soc. Am.*, vol. 106, no. 5, pp. 2653–2660, 1999. [Online]. Available: http://scitation.aip.org/content/asa/journal/jasa/106/5/10.1121/1.428095

[57] R.-E. Plessix, "A review of the adjoint-state method for computing the gradient of a functional with geophysical applications," *Geophys. J. Int.*, vol. 167, no. 2, pp. 495–503, 2006. [Online]. Available: http://dx.doi.org/10.1111/j.1365-246X.2006.02978.x

[58] J. Virieux and S. Operto, "An overview of full-waveform inversion in exploration geophysics," *Geophysics*, vol. 74, no. 6, pp. WCC1–WCC26, 2009. [Online]. Available: http://dx.doi.org/10.1190/1.3238367

[59] C. Li, N. Duric, and L. Huang, "Breast ultrasound tomography with total-variation regularization," in *Proc. SPIE*, vol. 7265, 2009, pp. 726 506–726 506–8.

[60] J. Jose, R. G. H. Willemink, W. Steenbergen, C. H. Slump, T. G. van Leeuwen, and S. Manohar, "Speed-of-sound compensated photoacoustic tomography for accurate imaging," *Med. Phys.*, vol. 39, no. 12, pp. 7262–7271, 2012.

[61] F. Anis, Y. Lou, A. Conjusteau, R. Su, T. Oruganti, S. A. Ermilov, A. A. Oraevsky, and M. A. Anastasio, "Investigation of the adjoint-state method for ultrasound computed tomography: a numerical and experimental study," in *Proc. SPIE*, vol. 8943, 2014, pp. 894 337–894 337–6. [Online]. Available: http://dx.doi.org/10.1117/12.2042636

[62] J. A. Sethian, "A fast marching level set method for monotonically advancing fronts," *Proceedings of the National Academy of Sciences*, vol. 93, no. 4, pp. 1591–1595, 1996. [Online]. Available: http://www.pnas.org/content/93/4/1591.abstract

[63] R. H. Byrd, P. Lu, J. Nocedal, and C. Zhu, "A limited memory algorithm for bound constrained optimization," *SIAM J. Sci. Comput.*, vol. 36, pp. 667–695, 199.

[64] M. Born and E. Wolf, *Principles of optics: electromagnetic theory of propagation, interference and diffraction of light*. CUP Archive, 1999.

TABLES

TABLE I: Parameters of the numerical breast phantom

Structure index	Tissue type	Sound speed [mm·μs^{-1}]	Slope of attenuation [dB·(MHz)$^{-y}$·cm^{-1}]
0	Adipose	1.47	0.60
1	Parenchyma	1.51	0.75
2	Benign tumor	1.47	0.60
3	Benign tumor	1.47	0.60
4	Cyst	1.53	0.00217
5	Malignant tumor	1.565	0.57
6	Malignant tumor	1.565	0.57
7	Malignant tumor	1.57	0.57

TABLE II: Parameters of the experimental breast phantom

Material	Sound speed [mm·μs^{-1}]	Attenuation coefficient at 2.5 MHz [dB/cm]
Fat	1.467	0.48
Parenchymal tissue	1.552	0.89
Cancer	1.563	1.20
Fibroadenoma	1.552	0.52
Gelatin cyst	1.585	0.16

FIGURES
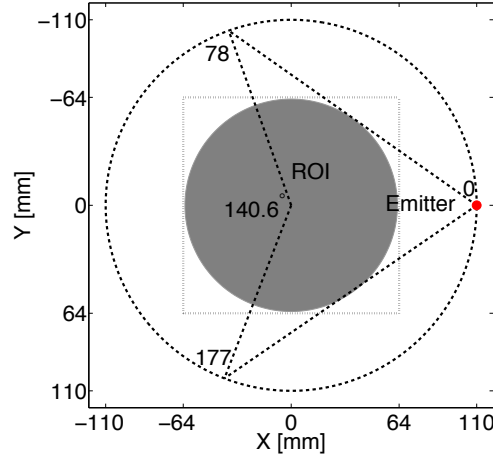
Fig. 1: Schematic of a USCT system with a circular transducer array whose elements are indexed from 0 to 255. It shows the first data acquisition, where element-0 (in red) is emitting an acoustic pulse, while all 256 elements are receiving signals. The region-of-interest (ROI) is shaded in gray, and the dashed square box represents the physical dimensions (128×128 mm^2) of all reconstructed images.
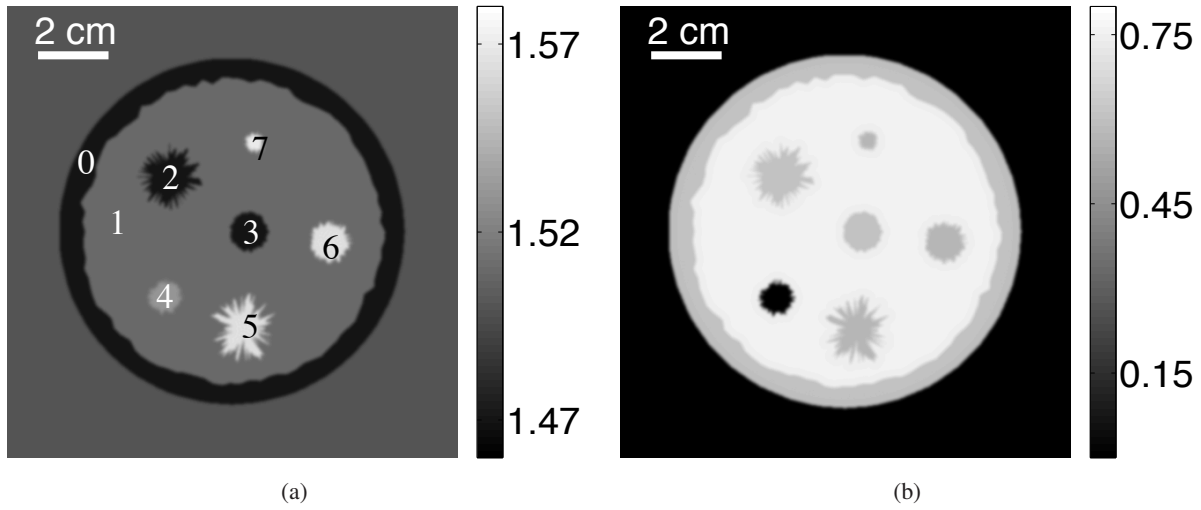
Fig. 2: (a) Sound speed map [mm·μs^{-1}] and (b) acoustic absorption coefficient map [dB·(MHz)$^{-y}$·cm^{-1}] of the numerical breast phantom.
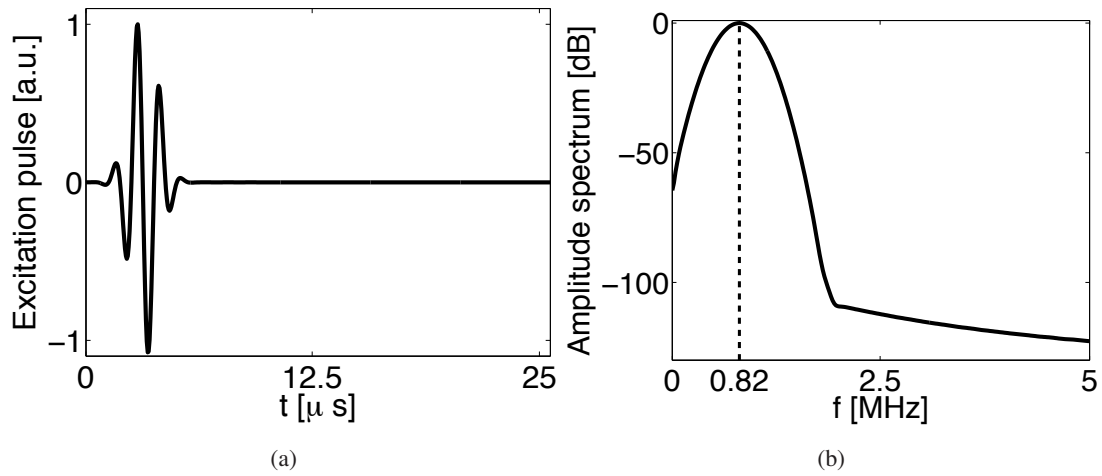
Fig. 3: (a) Normalized temporal profile and (b) amplitude spectrum of the excitation pulse employed in the computer-simulation studies. The dashed line in (b) marks the center frequency of excitation pulse at 0.82 MHz.

(a)

(b)

(c)
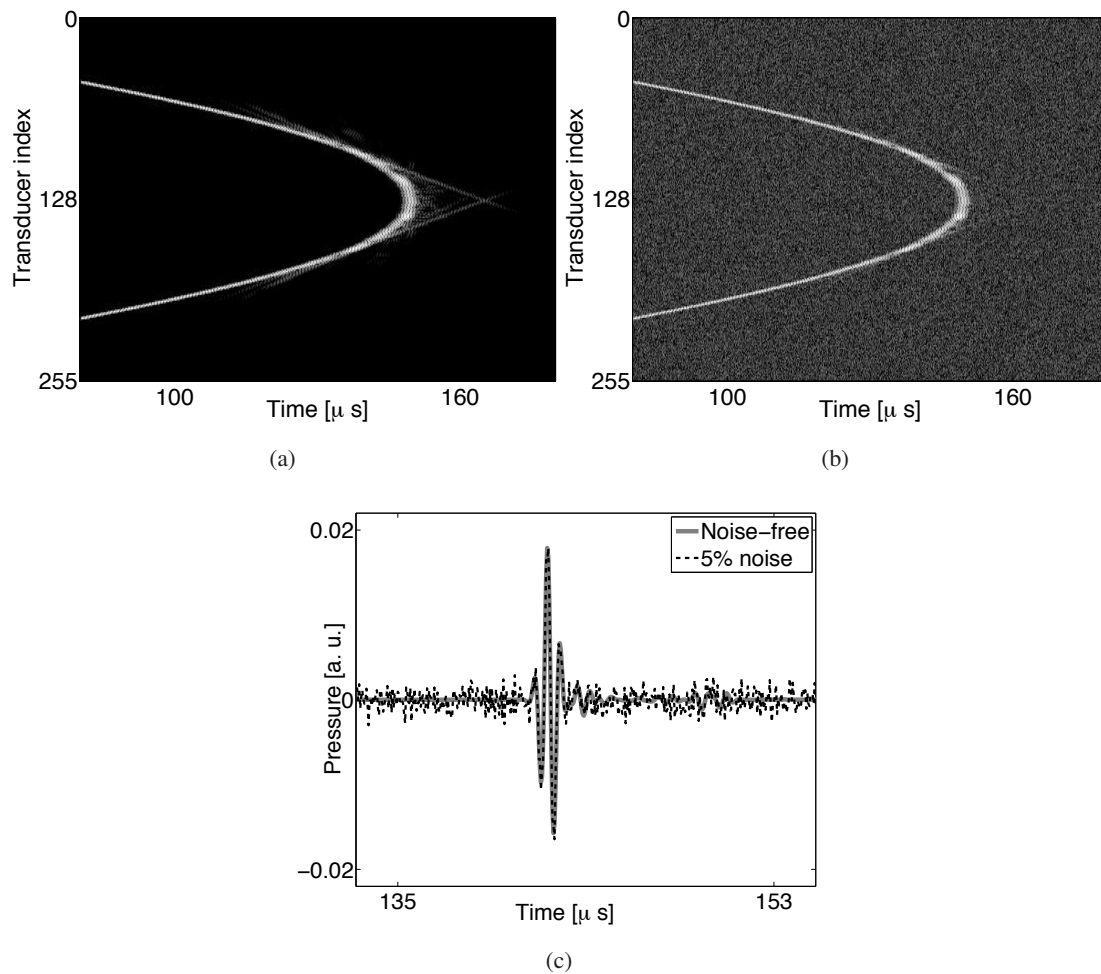
Fig. 4: Computer-simulated (a) noise-free and (b) noisy data vectors at the 0-th data acquisition. (c) Profiles of the pressure received by the 128-th transdcuer. The grayscale window for (a) and (b) is $[-45, 0]$ dB.
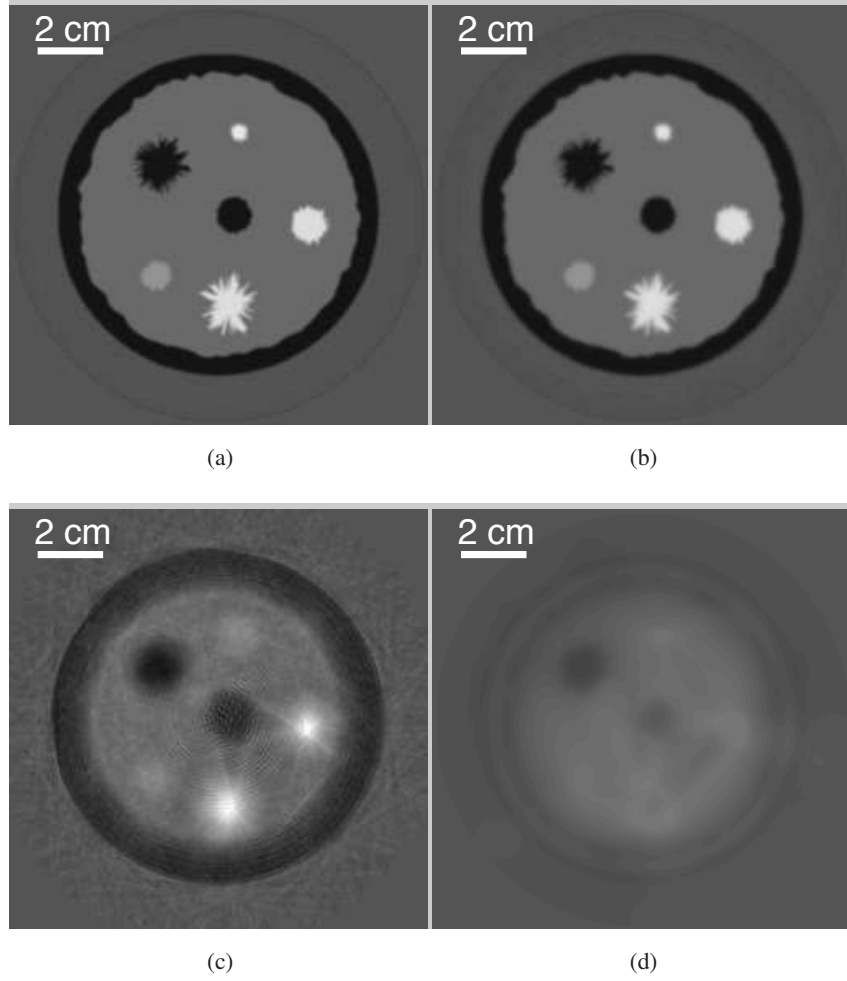
Fig. 5: Images reconstructed by use of (a) the WISE method after the 199-th iteration ($1,018$ runs of the numerical solver), (b) the sequential waveform inversion algorithm after the 43-rd iteration ($57,088$ runs of the numerical solver), (c) the bent-ray model-based sound speed reconstruction method, and (d) the sequential waveform inversion algorithm after the 1-st iteration ($1,024$ runs of the numerical solver) from the noise-free non-attenuated data. The grayscale window is $[1.46, 1.58]$ mm/μs.
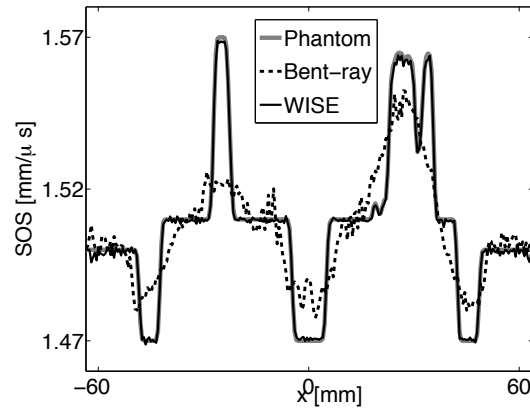
Fig. 6: Profiles at $y = 6.5$ mm of the images reconstructed by use of the bent-ray TOF image reconstruction method and the WISE method from the noise-free non-attenuated data.

(a)

(b)

(c)

(d)
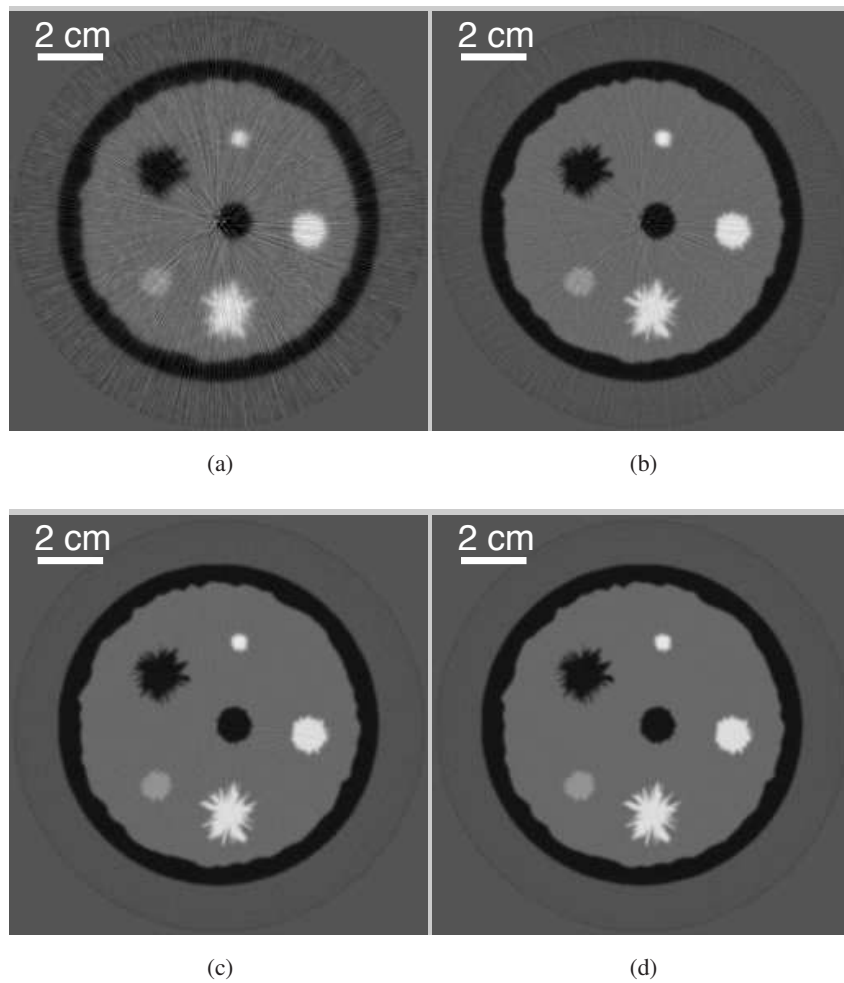
Fig. 7: Images reconstructed by use of the WISE method after (a) the 20-th, (b) the 50-th, (c) the 100-th, and (d) the 250-th iteration from the noise-free, non-attenuated data set. The grayscale window is $[1.46, 1.58]$ mm/μs.
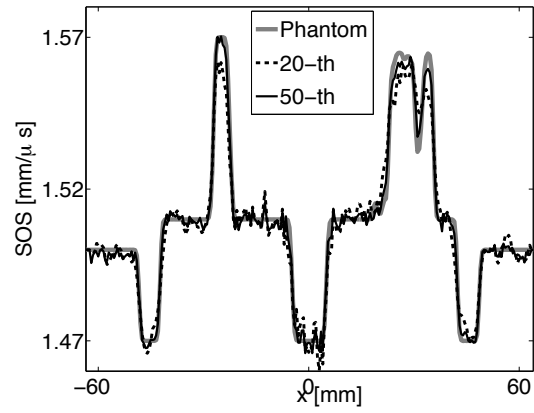
Fig. 8: Profiles of the images reconstructed by use of the WISE method from the noise-free non-attenuated data after different numbers of iterations.
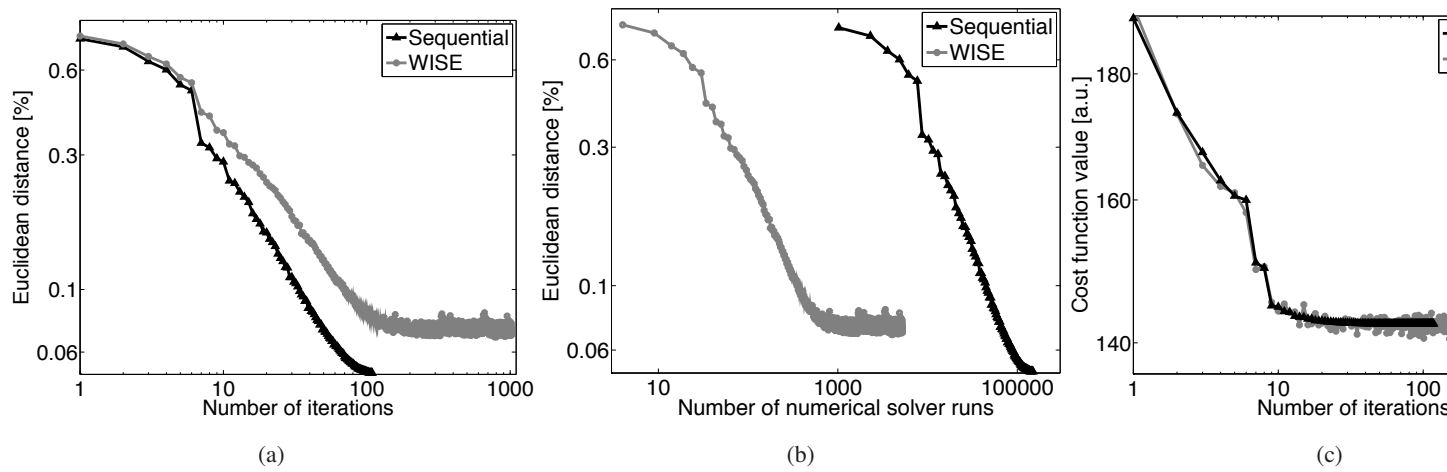
Fig. 9: Plots of the absolute Euclidean distances versus (a) the number of iterations and (b) the number of numerical solver runs. (c) Plots of the cost function value versus the number of iterations.
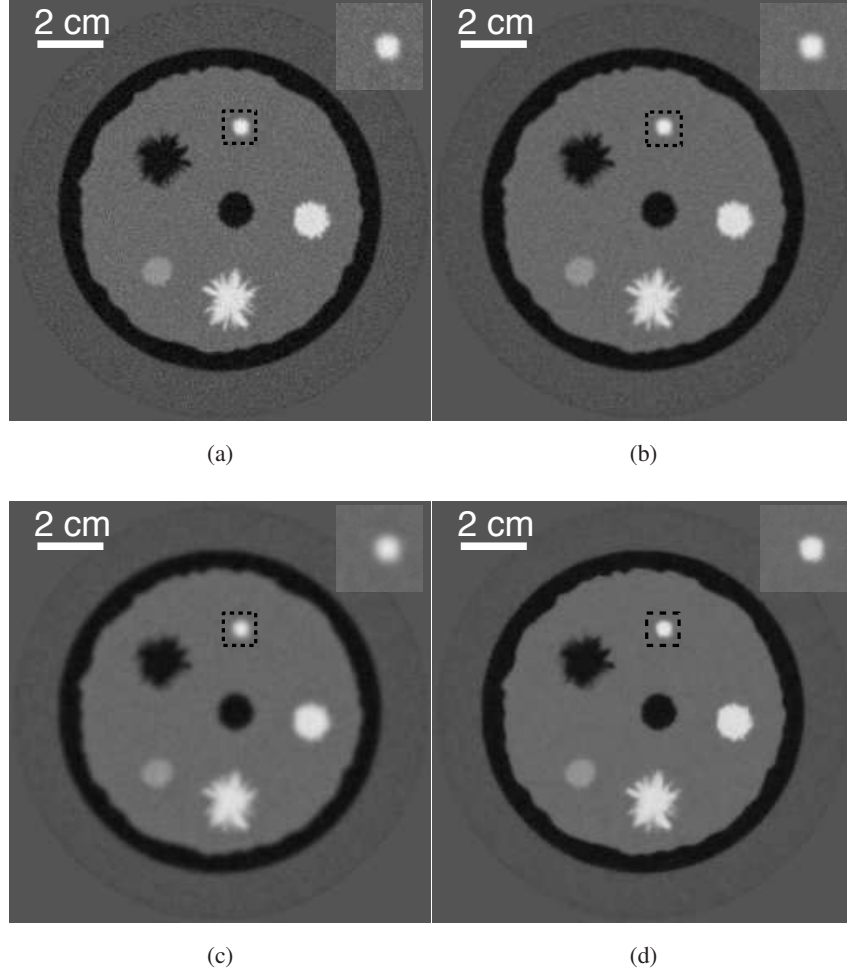
Fig. 10: Images reconstructed from non-attenuated data contaminated with Gaussian random noise. Images (a-c) were reconstructed by use of the WISE method with a quadratic penalty with $\beta^{\mathrm{Q}} = 1.0 \times 10^{-3}$, 1.0×10^{-2}, and 1.0×10^{-1}, respectively. Image (d) was reconstructed by use of the WISE method with a TV penalty with $\beta^{\mathrm{TV}} = 5.0 \times 10^{-4}$. The insert in the up right corner of each image is the zoomed-in image of the dashed black box. The grayscale window is $[1.46, 1.58]$ mm/μs.
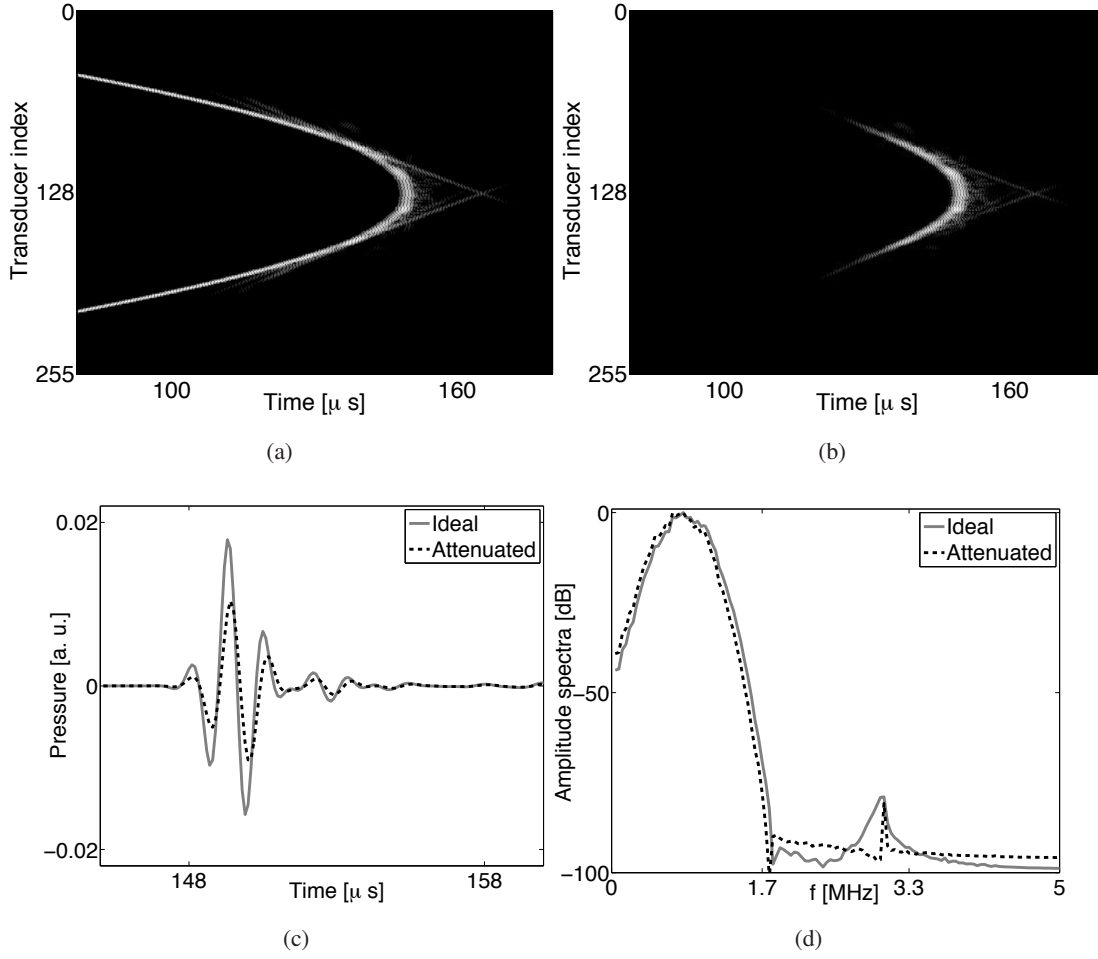
Fig. 11: (a) Computer-simulated noise-free attenuated pressure of the 0-th data acquisition. (b) The difference between the attenuated pressure data and the non-attenuated pressure data. (c) The temporal profiles and (d) the amplitude spectra of the pressure received by the 128-th transducer. The grayscale window for (a) and (b) is $[-45, 0]$ dB.
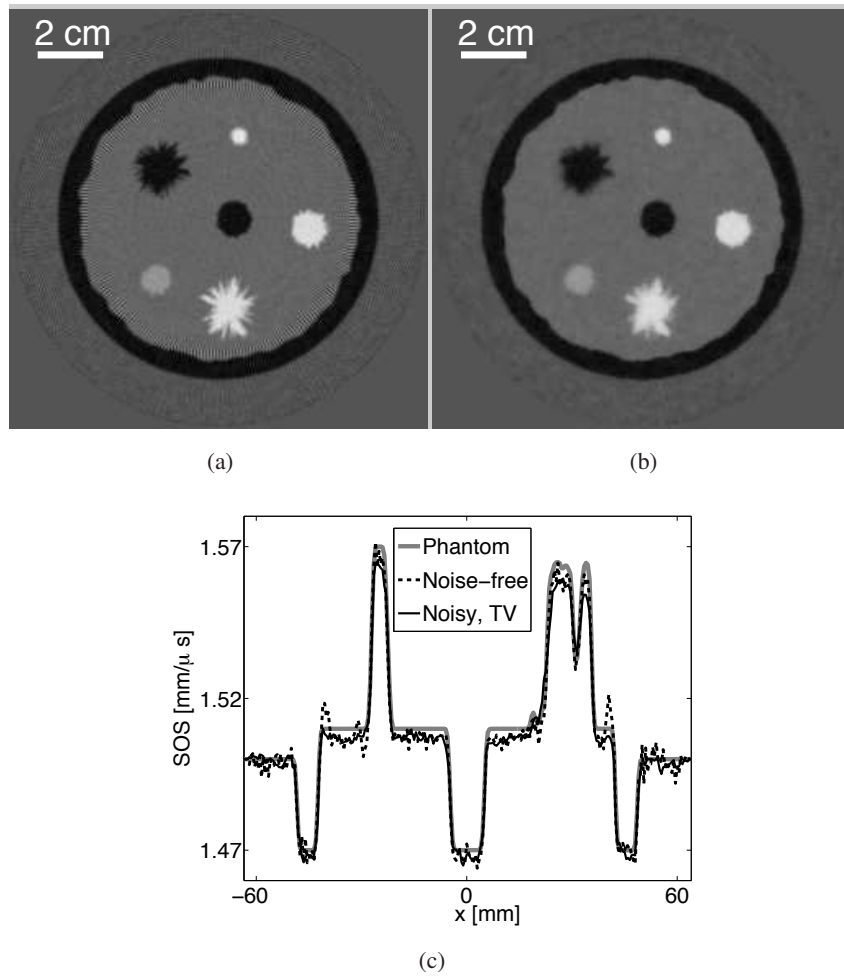
Fig. 12: (a) Image reconstructed by use of the WISE method from the noise-free attenuated data. (b) Image reconstructed by use of the WISE method with a TV penalty with $\beta^{\mathrm{TV}} = 5.0 \times 10^{-4}$, from the noisy attenuated data. The grayscale window is $[1.46, 1.58]$ mm/μs. (c) Profiles at $y = 6.5$ mm of the reconstructed images.
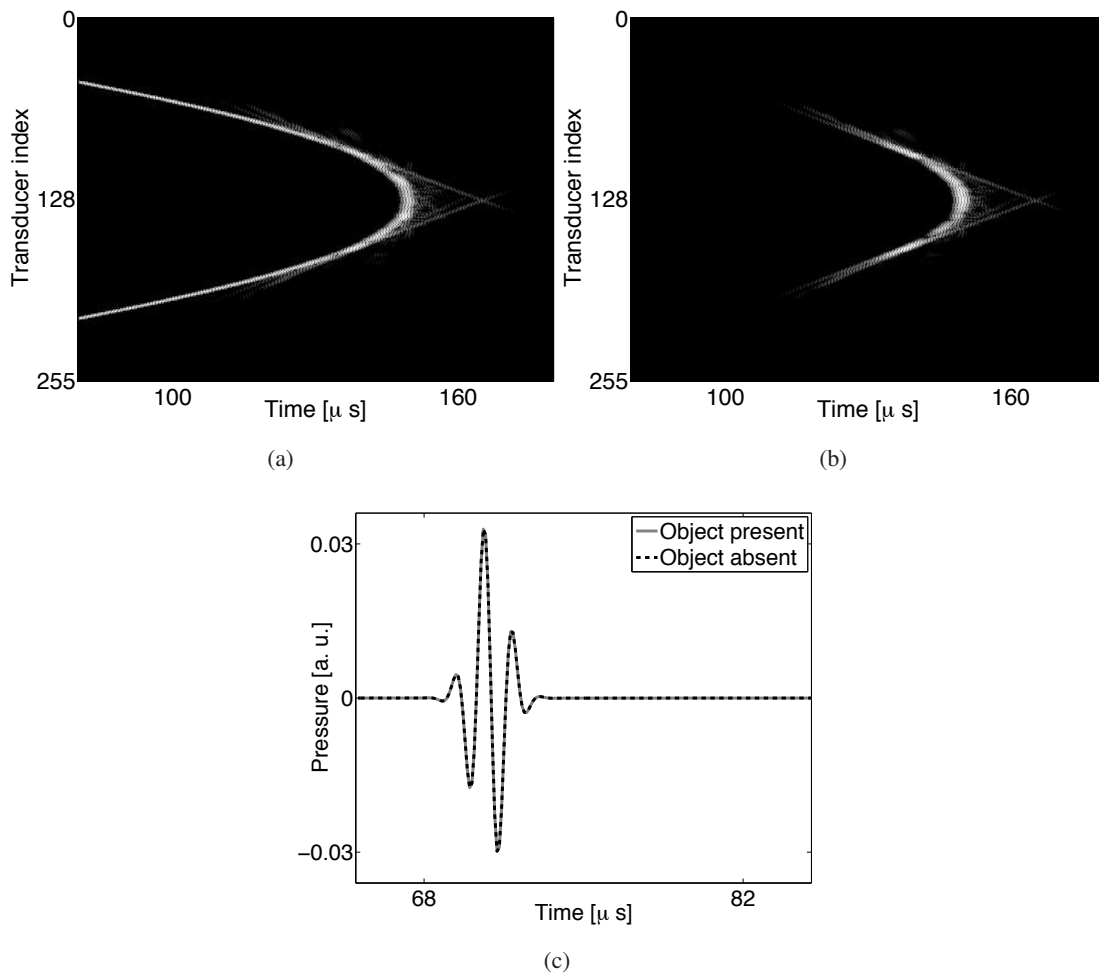
Fig. 13: (a) Computer-simulated noise-free non-attenuated pressure data when the object is absent. (b) The difference between the pressure data when object is present and the pressure data when the object is absent. (c) Profiles of the pressure received by the 40-th transducer. The grayscale window for (a) and (b) is $[-45, 0]$ dB.

(a)

(b)

(c)
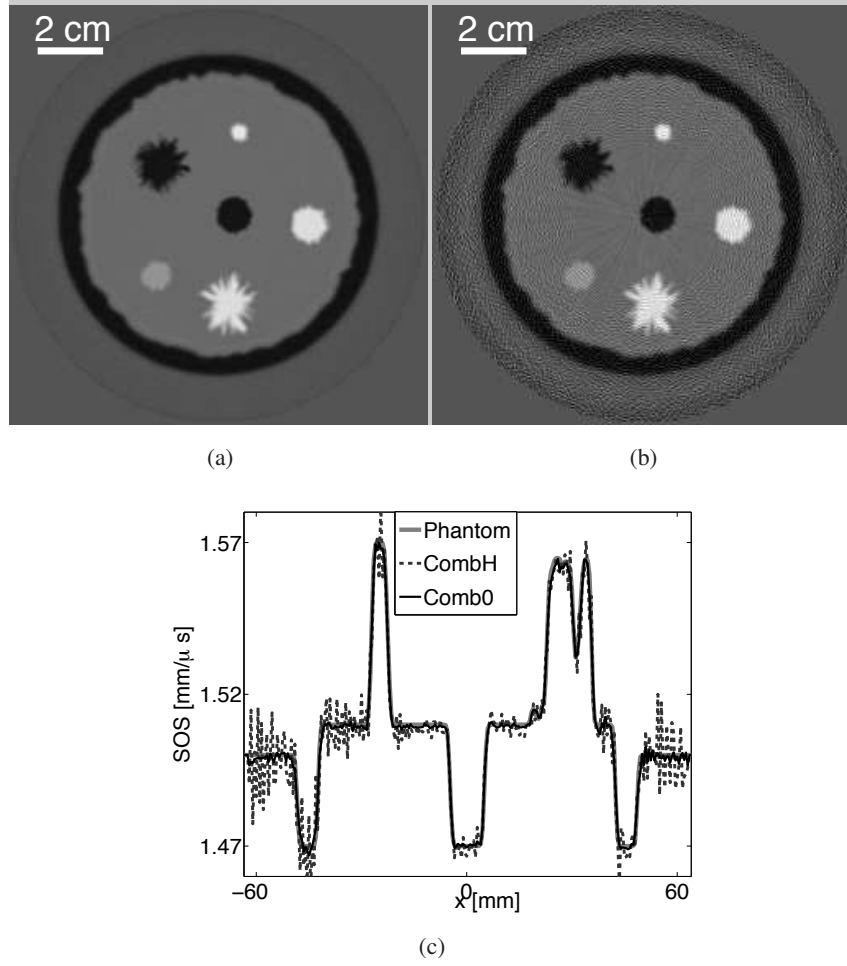
Fig. 14: Images reconstructed by use of the WISE method from noise-free combined data that are completed (a) with computer-simulated pressure corresponding to a homogeneous medium and (b) with zeros. The grayscale window is $[1.46, 1.58]$ mm/μs. (c) Profiles at $y = 6.5$ mm of the images reconstructed by use of the WISE method from the two combined data sets.
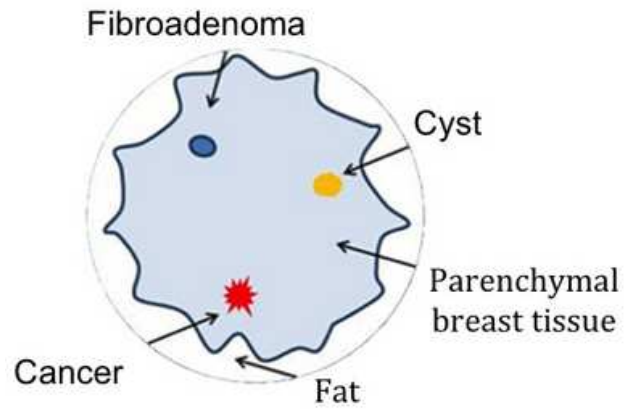
Fig. 15: Schematic of the breast phantom employed in the experimental study.
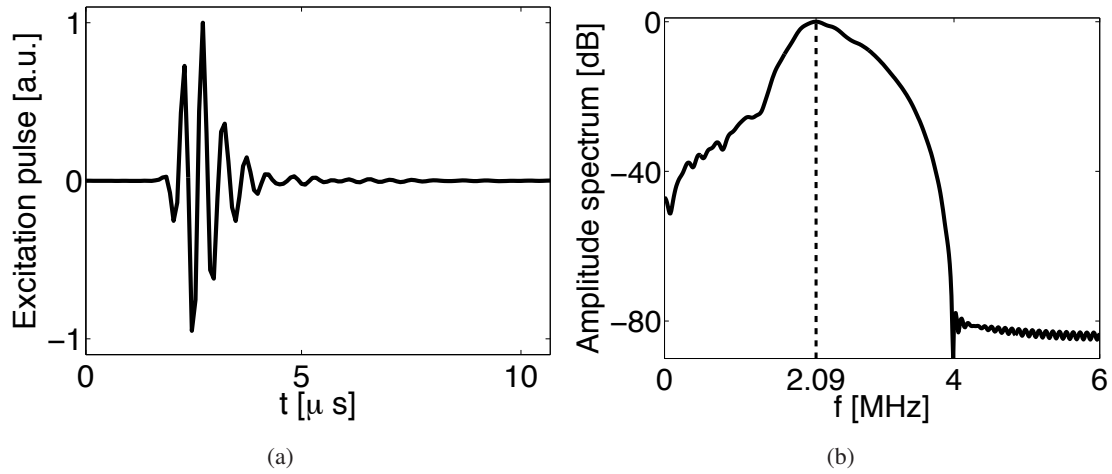
Fig. 16: (a) Normalized temporal profile and (b) amplitude spectrum of the excitation pulse employed in the experimental studies. The dashed line in (b) marks the center frequency of excitation pulse at 2.09 MHz.
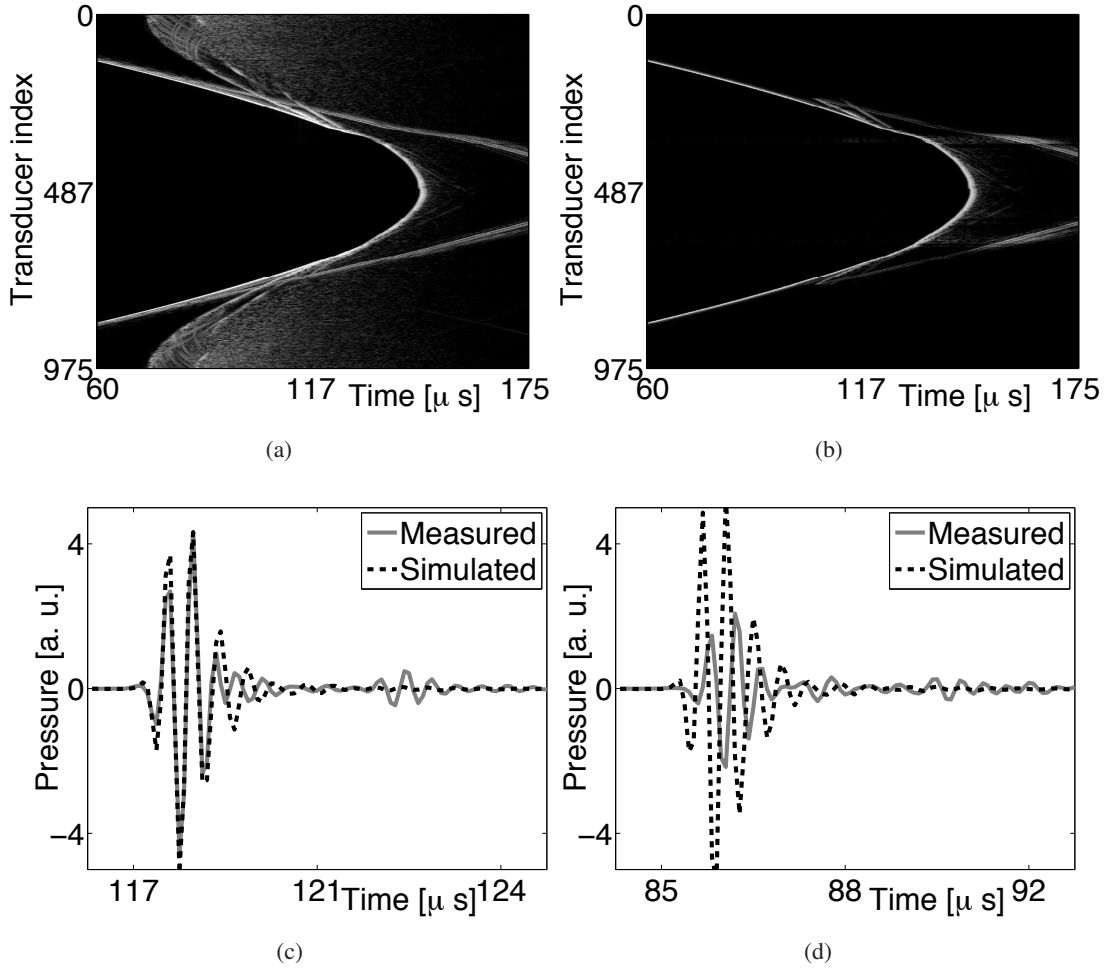
Fig. 17: Zeroth acquisition of (a) the experimentally-measured raw data and (b) the combined data, respectively, and time traces at the 0-th acquisition received by (c) the 300-th receiver, and (d) the 200-th receiver, respectively. The grayscale window for (a) and (b) is $[-45, 0]$ dB.
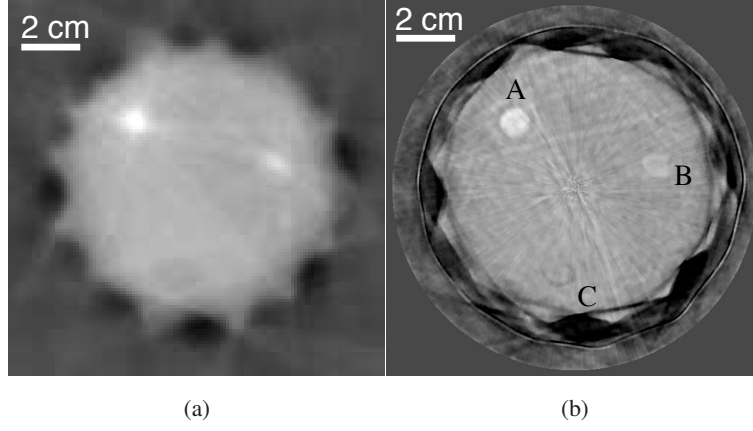
Fig. 18: Images reconstructed from the experimentally measured phantom data by use of (a) the bent-ray model-based sound speed reconstruction method and (b) the WISE method with a TV penalty with ($\beta^{\mathrm{TV}} = 1.0 \times 10^2$) after the 200-th iteration. The grayscale window is $[1.49, 1.57]$ mm/μs.
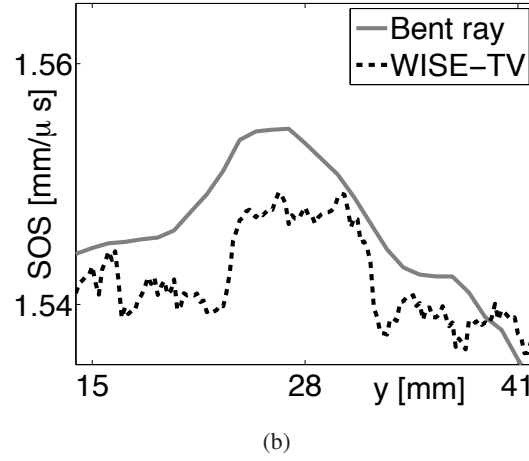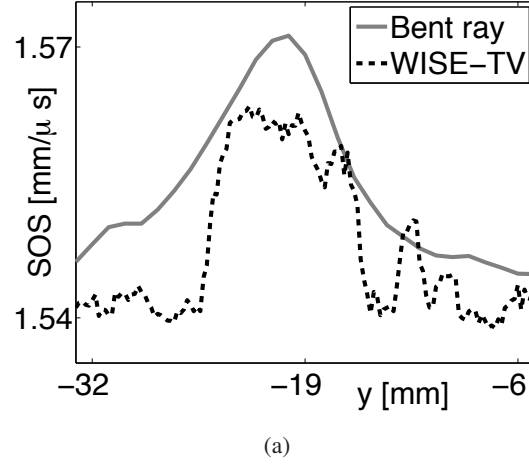
(a)

(b)

Fig. 19: Profiles at (a) $x = -24.0$ mm and (b) $x = 10.0$ mm of the reconstructed images by use of the bent-ray model-based sound speed reconstruction method (light solid) and the WISE method with a TV penalty with $\beta^{\mathrm{TV}} = 1.0 \times 10^2$ (dark dashed) from experimentally measured data.
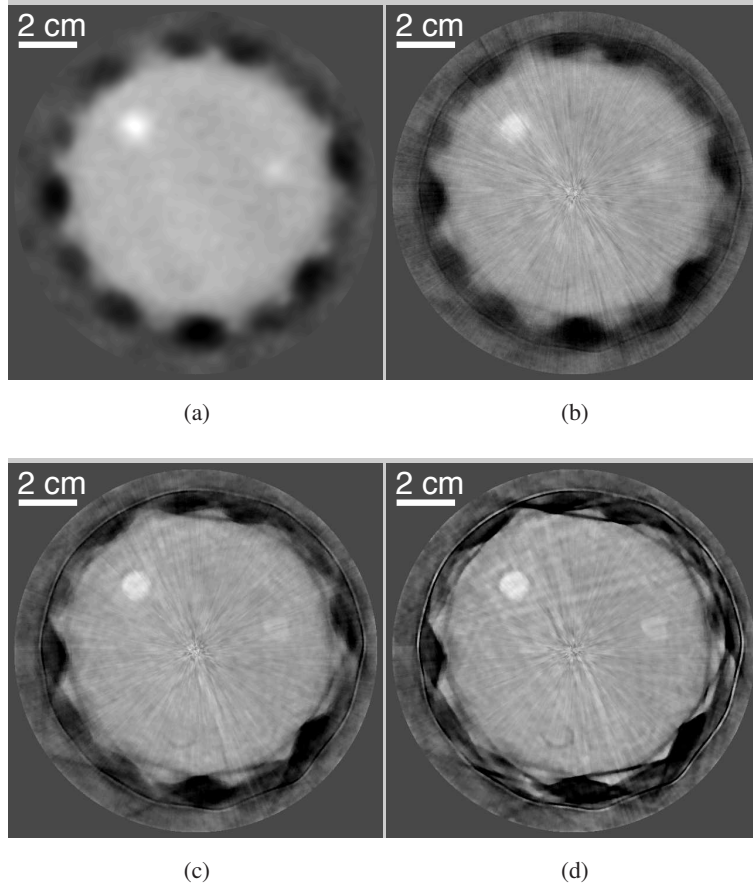
Fig. 20: (a) The initial guess of the sound speed map and the images reconstructed by use of the WISE method with a TV penalty with ($\beta^{\mathrm{TV}} = 1.0 \times 10^2$) after (b) the 10-th, (b) the 50-th and (d) the 300-th iteration, from the experimentally measured phantom data. The grayscale window is $[1.49, 1.57]$ mm/μs.

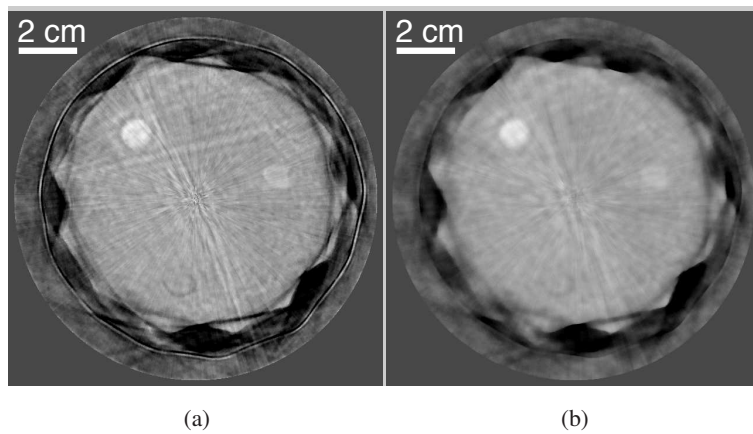(a)   (b)

Fig. 21: Images reconstructed by use of the WISE method with a TV penalty with (a) $\beta^{\text{TV}} = 5.0 \times 10^1$, and (b) $\beta^{\text{TV}} = 5.0 \times 10^2$, from the experimentally measured phantom data. The grayscale window is $[1.49, 1.57]$ mm/μs.